3-18-2019

Optimization of Quantum Optical Metrology Systems

Nicholas Michael Studer

Recommended Citation

OPTIMIZATION OF QUANTUM OPTICAL METROLOGY SYSTEMS

A Dissertation

Submitted to the Graduate Faculty of the
Louisiana State University and
Agricultural and Mechanical College
in partial fulfillment of the
requirements for the degree of
Doctor of Philosophy

in

The Department of Physics & Astronomy

by
Nicholas Michael Studer
B.S. Physics, University of New Orleans, 2014
May 2019

To my dog.

Acknowledgments

Table of Contents

List of Figures

Abstract

It can be said that all of humanity's efforts can be understood as a problem of optimization. We each have a natural sense of what is "good" or "bad" and thus our actions tend towards maximizing – or optimizing – some notion of good and minimizing those things we perceive as bad or undesirable.

Within the sciences, the greatest form of good is knowledge. It is this pursuit of knowledge that leads to not only life-saving innovations and technology, but also to furthering our understanding of our natural world and driving our philosophical pursuits.

The principle method of obtaining knowledge in the sciences is by performing measurements; the simple act of comparing one attribute of a system to a known standard and recording the observed value is how all scientific progress is made. The act of performing measurements is in fact so important that there is an entire field of study surrounding it: metrology. One critical component of metrology is the development of new techniques to perform measurements, or alternative measurement schemes that are more optimal in some way. This is where there is room to exploit quantum physics to improve our techniques – we can perform quantum metrology.

In quantum mechanics we routinely deal with the smallest, weakest, most delicate of systems. Quantum properties are inherently very sensitive to their environment; this of course makes them highly intolerant of noise but also makes them great resources to perform sensitive measurements. Quantum metrology concerns itself with utilizing quantum phenomena to extract more information from the natural world than is possible by conventional, or classical, means.

To perform optimal measurements, these quantum systems must of course be optimal by some metric. Performing the "optimal" measurement requires several ingredients. First, we need the optimal tools or instrumentation. In quantum mechanical language, this means we need the optimal probe state. Then, we need to optimize the interaction of our instrumentation with the system we which to interrogate so that we can extract the desired information.

This translates to needing the best possible interaction between the probe state and the system in question – in other words, we need to optimize the evolution of the probe. Finally, we must take care to extract the most information as possible at the output; we must not neglect any information present in the evolved probe state.

The entire quantum metrology process can be summarized as thus: probe state preparation, probe state evolution, and evolved state detection. These elements make up the basis of this thesis. Within, I will discuss several works in which I optimize the performance of systems that implement these metrology elements. Specifically, I will first discuss one such system in which I optimize the probe interrogation of the phase, i.e. perform phase-estimation, in a Boson-sampling device. Then, I will show some strategies to progressively build up highly-useful Fock states starting from single photons as a resource. Lastly, I show how to utilize quantum properties of quantum light (specifically, squeezed light) to accurately calibrate a single-photon detector without need for a reference detector.

1 Introduction

The goal of optimization is to enhance or maximize desired features, and suppress or minimize the irrelevant or bothersome features. In performing measurements, we want to perform the most accurate and precise measurements as possible. In order to obtain the best measurements, we need to minimize the fluctuations or noise. In other words, we aim for a high signal-to-noise ratio (SNR). Not only do we want high SNR measurements, we want to use as few resources as necessary – and no more. Quantum mechanics gives us the tools we need to perform highly-precise measurements using fewer resources than classical measurement systems can achieve. Resource-management is extremely important for many applications in which higher-power metrology systems are unrealistic or even detrimental to achieving precision. For example, sensitive range-finding applications may not want to alert the targets that they are being observed. Microorganisms may not survive probing by high-intensity lasers. If nothing else, power is expensive; using more power is something that we should seek to avoid when possible. We should strive to maximize the use of the tools we have – make sure that we are doing *intelligent* measurements to obtain and extract information about the systems of interest. Using the language of quantum optics and quantum metrology, we can accurately keep track of our fundamental resources and describe limits to the precision nature allows us to probe physical systems. In this section I will develop the tools necessary to understand the generic quantum phase-estimation problem, which nicely describes any system that can be mapped to an interferometer. The concepts in this section will be necessary to understand the rest of this manuscript, which constitutes the bulk of my research.

1.1 Quantum Optics

1.1.1 States of Light

Here I will outline the primary quantum states of light, particularly those that see frequent use throughout this document. I will introduce them here at a high level only, since I have not yet covered some of the more complex aspects of quantum light such as photon statistics,

quadrature variance, entanglement, etc., This section serves to introduce the primary "tool-kit" for the general quantum optical metrology system.

If optics is the (classical) study of light described by alternating electric and magnetic fields, then quantum optics is the study of the photon – the discrete (quantized) excitations of the electromagnetic (EM) field. We can describe the action of these excitations in the language of creation and annihilation operators $\hat{a}^\dagger$ and $\hat{a}$, respectively. These non-commuting operators obey the relation

$$[\hat{a}^\dagger, \hat{a}] = 1, \tag{1.1}$$

and the product of these operators $\hat{a}^\dagger \hat{a} = \hat{n}$ represents the photon-number operator, which contains information about the mean number of excitations in any quantum state. States containing multiple excitations are denoted $|n\rangle$ and are referred to as the Fock states. These are eigenstates of the number operator $\hat{n}$ and thus obey $\hat{n}|n\rangle = n|n\rangle$. We also have the actions of $\hat{a}^\dagger$ and $\hat{a}$ on these states

$$\begin{aligned}
\hat{a}|n\rangle &= \sqrt{n}|n-1\rangle, \\
\hat{a}^\dagger|n\rangle &= \sqrt{n+1}|n+1\rangle,
\end{aligned} \tag{1.2}$$

which highlights the natural interpretation of $\hat{a}^\dagger$ and $\hat{a}$ as "creating" and "annihilating" photons from the field, respectively. Fock states are highly-quantum fields, having no classical analogue, and exhibit very interesting properties that will give rise to quantum effects we will exploit throughout this work to obtain useful new results.

Since photons are excitations of the EM field, quantum mechanics tells us that we can have a state of no excitations at all – that which contains zero photons [1]. This state is the vacuum state $|0\rangle$, and the action of $\hat{a}^\dagger$ on this field creates the single-photon state $|1\rangle$, as is apparent from Eq 1.2. This state is also a strictly quantum state, and is part of every theoretical quantum-optician's primary toolkit. Many of the results in this work will highlight the single photon, and how we can exploit it to enable new techniques in the

science of performing measurements.

One of the most commonly-employed states in quantum optics is laser light. In the language of quantum optics we refer to this light as the coherent state, denoted $|\alpha\rangle$. It is typically defined as the eigenstate of the annihilation operator obeying $\hat{a}|\alpha\rangle = \alpha|\alpha\rangle$. The complex eigenvalue α contains information about the power and phase of the laser. This state, though generated through highly quantum mechanical processes, is often considered to be on the border of the quantum-classical realms. For the purposes of this document, we will discuss only the effects of the coherent state on $\chi^{(2)}$ nonlinear crystals. This interaction produces a highly-useful quantum state known as two-mode squeezed vacuum (TMSV).
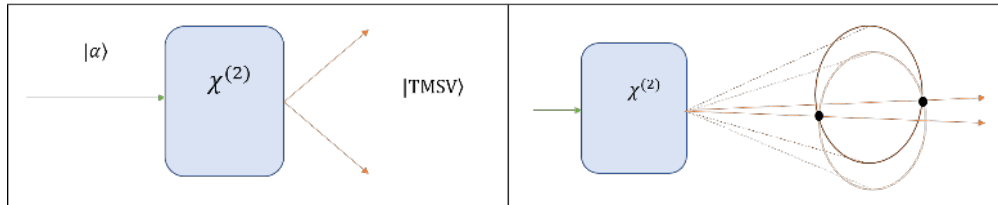
Figure 1.1. Left: Generation of two-mode squeezed vacuum light by illumination of a χ^2 nonlinear crystal with laser light. Right: Overlapping cones in Type-II SPDC produce identical pairs of photons.

When coherent light interacts with a χ^2 nonlinear crystal, birefringence effects results in the light being emitted in two cones from the opposite side of the crystal. This process is called spontaneous parametric down-conversion (SPDC), of which there are two types. Type II SPDC (shown in Fig. 1.1) occurs when the two emitted cones of light have two points of overlap. At these points, you can find completely identical photons that form an entangled state. This extremely unique state is denoted $|\xi\rangle$ and is useful for a range of applications in quantum technology, two of which will be discussed in this manuscript.

The final state I will introduce is the most widely-known and understood state of light: the thermal state. This is a highly-classical state; in fact, the thermal state cannot be written as a ket because it is not a pure quantum state. Typically denoted $\hat{\rho}_{\text{th}}$, this state is a classical probabilistic mixture of Fock states, with the vacuum state contributing the bulk of the likelihood. This state of light is produced by blackbody radiation, which comes about

as a result of physical matter being at temperatures greater than 0 K. This light, despite its classical nature, is ever-present in our universe and can be understood in quantum optics terminology. Therefore, it is an extremely important state to understand.

With these states, we can observe many interesting quantum phenomena that lead to startling results and, in particular, new and enhanced methods of performing measurements. In order to understand why some states of light are "better" or "more quantum" than others (especially for metrology), we typically need only to understand the photon-number statistics of the light in question.

1.1.2 Statistics of quantum light

An arbitrary quantum state can be represented as a superposition of Fock states $|n\rangle$, which form a complete orthonormal basis such that $\langle n|m\rangle = \delta_{n,m}$ and $\sum |n\rangle\langle n| = \hat{I}$, the identity matrix. Thus we can expand an arbitrary pure quantum state $|\Psi\rangle$ as

$$|\Psi\rangle = \sum_{n=0}^{\infty} c_n |n\rangle, \tag{1.3}$$

where each c_n represents the complex probability amplitude of the nth Fock state, and the absolute-value squared of each c_n corresponds to the real probability P_n to observe state $|n\rangle$ upon measurement.

$$|c_n|^2 = P_n, \tag{1.4}$$

Of course, upon measuring $|\Psi\rangle$, you must observe *some* Fock state $|n\rangle$. Thus we require $\sum P_n = 1$ as well.

If one knows the values of all c_n in a Fock-state expansion, that state is uniquely-defined up to a global phase term which plays no role in observable physics. Of the states discussed in Sec. 1.1.1, we have the following distributions:

4

$$\text{Vacuum: } c_n = \delta_{n,0},$$

$$\text{Single-photon: } c_n = \delta_{n,1},$$

$$\text{Fock: } c_n = \delta_{n,m},$$

$$\text{Coherent: } c_n = e^{-\frac{1}{2}|\alpha|^2} \frac{\alpha^n}{\sqrt{n!}},$$

$$\text{TMSV: } c_{n,m} = \frac{(-1)^n e^{in\theta}}{\cosh r}(\tanh r)^n \delta_{n,m},$$

$$\text{Thermal: } P_n = \frac{\bar{n}^n}{(1+\bar{n})^{n+1}}. \tag{1.5}$$

One can quickly observe from Eq. 1.5 that these states have drastically different distributions in Fock space. The "least quantum" state, the thermal state, has a Gaussian distribution parameterized by $\bar{n}$, which represents the mean-photon number of the state and is a function of the temperature of the object. Meanwhile, the "borderline" state $|\alpha\rangle$ is Poissonian-distributed – this in fact illustrates why laser light is able to perform measurements at a more precise level than thermal light. The fluctuations in coherent light are inherently smaller than that of thermal light, giving rise to a lower noise floor. This becomes apparent in the Wigner phase-space picture.

To introduction the Wigner representation of quantum light, we must first express the states in terms of their position and momentum quadratures. Classically, Maxwell's equations give rise to light as oscillating electric and magnetic fields – $\vec{E}(\vec{r}, t)$ and $\vec{B}(\vec{r}, t)$, respectively. We can quantize these fields as

$$\hat{E}_x(z, t) = E_0(\hat{a} + \hat{a}^\dagger) \sin kz,$$

$$\hat{B}_y(z, t) = -iB_0(\hat{a} - \hat{a}^\dagger) \cos kz, \tag{1.6}$$

where the creation and annihilation operators have the form

$$\hat{a} = (2\hbar\omega)^{-1/2}(\omega\hat{q} + i\hat{p}),$$

$$\hat{a}^\dagger = (2\hbar\omega)^{-1/2}(\omega\hat{q} - i\hat{p}), \tag{1.7}$$

and $\hat{q}$ and $\hat{p}$ are the canonical momentum and position operators, respectively, obeying $[\hat{q},\hat{p}] = i\hbar$. Note that $\hat{q}$, $\hat{p}$ as well as $\hat{a}$, $\hat{a}^\dagger$ contain roughly the same information about the state, as they are linear transformations of each other. Then we can express any state $\hat{\rho}(\hat{q},\hat{p})$ in terms of its phase-space representation by applying the Wigner-Weyl transform [2]:

$$W(q,p) = \frac{1}{2\pi\hbar} \int_{-\infty}^{\infty} \langle q + \frac{1}{2}x|\hat{\rho}|q - \frac{1}{2}x\rangle e^{\frac{ipx}{\hbar}} \, dx. \tag{1.8}$$

Applying Eq. 1.8 to $|\psi\rangle = \sum_{n=0}^{\infty} c_n |n\rangle$ with the c_n given by Eq: 1.5 we can obtain the Wigner-function representation of the previously discussed states of light.

$$\text{Vacuum: } W(q,p) = \frac{1}{\pi} e^{-(p^2+q^2)},$$

$$\text{Single-photon: } W(q,p) = -\frac{1}{\pi}[1 - 2(p^2 + q^2)]e^{-(p^2+q^2)},$$

$$\text{Fock: } W(q,p) = \frac{1}{\pi}(-1)^n L_n[2(q^2 + p^2)]e^{-q^2-p^2},$$

$$\text{Coherent: } W(q,p) = \frac{1}{\pi} e^{-(q-\sqrt{2}|\alpha|\cos\theta)^2 - (p-\sqrt{2}|\alpha|\sin\theta)^2},$$

$$\text{TMSV: } W_{|\xi\rangle}(q_1,p_1,q_2,p_2) = \frac{1}{\pi^2} \exp[-\cosh 2r(q_1^2 + p_1^2 + q_2^2 + p_2^2) + 2\cos(\theta)\sinh 2r(q_1 q_2 - p_1 p_2) +$$

$$2\sin\theta \sinh 2r(q_1 p_2 + q_2 p_1)],$$

$$\text{Thermal: } W(q,p) = \frac{1}{\pi(2\bar{n} + 1)} e^{-\frac{q^2+p^2}{2\bar{n}+1}},$$

$$\tag{1.9}$$

where $L_n(x)$ is the n-th Laguerre polynomial. Note that the TMSV state has four quadrature operators because it is a two-mode state. The parameters r and θ represent the strength of the nonlinear crystal and the squeezing angle of the output beam, respectively. The mean photon number for the TMSV state is $\bar{n} = (\sinh r)^2$.

The Wigner representation serves especially useful in visualizing the quantum statistics of a state. By plotting the Wigner function, we immediately gain intuition into how "quantum" the state is.

In Fig. 1.2 we can see that there is quite the diversity in phase-space distributions
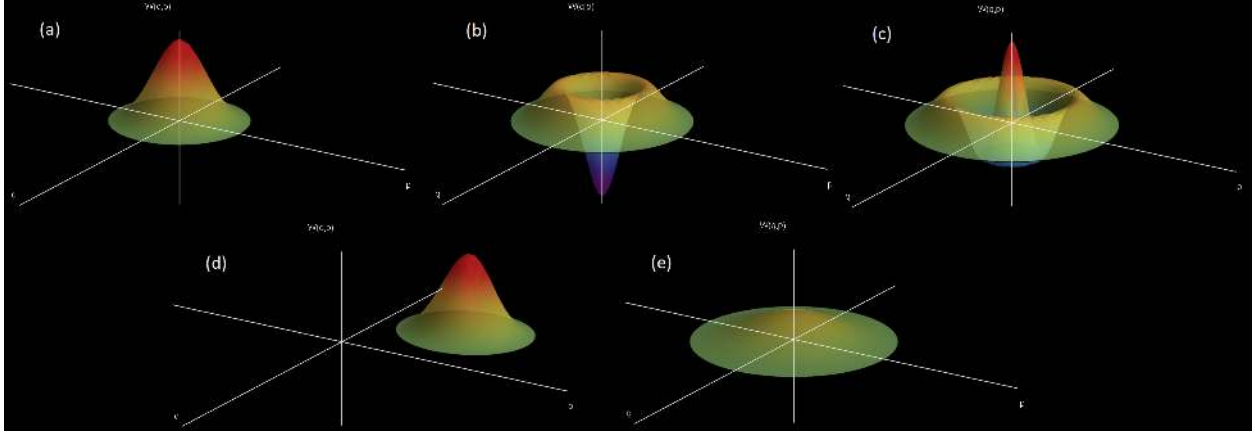
Figure 1.2. Wigner functions for (a) the vacuum state, (b) the single-photon state, (c) the two-photon state, (d) the coherent state with $\alpha = 2.5$ and $\theta = 3\pi/4$, and (e) the thermal state with $\bar{n} = 1$

among different states of light. There are several features to unpack here. Consistent with Eq: 1.5, we see the vacuum state 1.2(a), the coherent state 1.2(d), and the thermal state 1.2(e) are Gaussian. However, the thermal state has a much wider spread – this is in fact what makes it a lousy state for metrology purposes; the fluctuations in q, p are much larger than that of, for example, the coherent state. Though the vacuum state and the coherent state are similar in many ways, particularly in the fact that their spread in q, p is tightly contained (minimum, in fact), we can observe that the coherent state has a phase while the vacuum state does not. This phase comes as a result of the coherent state being displaced by the origin. The frequency of the coherent light dictates the speed at which the Gaussian packet revolves around the origin, and the resulting phase creates interference effects when two coherent states of differing phase are made to interact. Turning our attention to the Fock states 1.2(b) and 1.2(c), representing the single- and two-photon states, respectively, we see quite bizarre features compared to the Gaussian states. Most obviously, we see that the Wigner representation of the Fock states takes on negative values in phase space. This is why the Wigner function is considered a *quasi*-probability distribution. A state whose Wigner representation contains negative values is said to be strictly quantum [3], though the converse is not generally true.

7

1.1.3 Distinguishability and Entanglement

The last and potentially most unique aspect of quantum mechanics is entanglement. To properly illustrate what it means for two quantum states to be entangled, we will first discuss the idea of distinguishability.

Suppose we have a device which has two inputs and two outputs, and this device operates in a probabilistic way such that each input is sent to one of the outputs randomly but fairly, on average. In other words, after many trials, one input will come out of each output roughly half the time – as opposed to being biased towards one output or the other. In optics we refer to this device as a beamsplitter (BS), and we will use it to conduct a thought experiment that will illustrate how quantum mechanics lends itself to unintuitive behavior even in very simple situations.
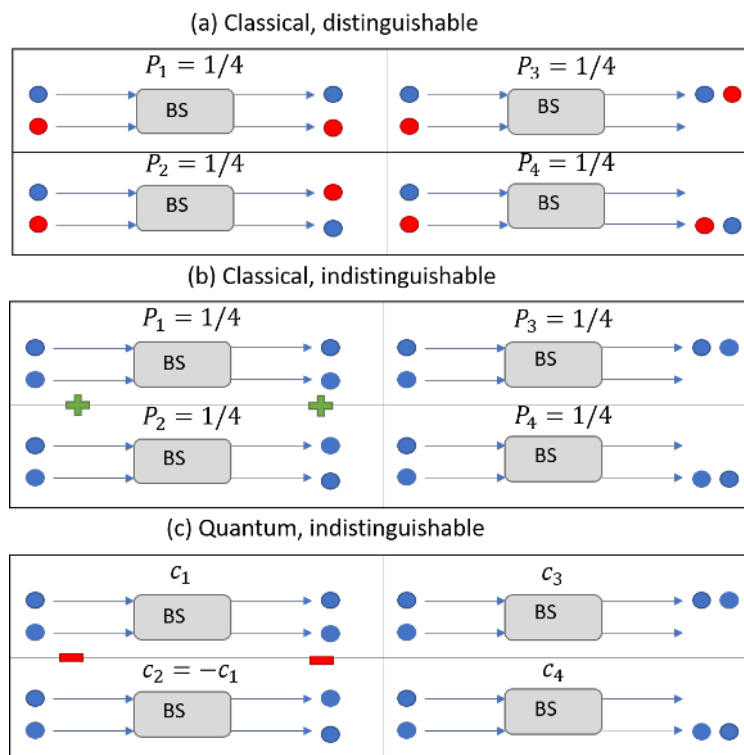
Figure 1.3. The probablities of a beamsplitter, for classical and quantum cases of distinguishability versus indistinguishability.

In a classical distinguishable scenario, a beamsplitter has four distinct possibilities, shown

in Fig 1.3(a). Then each outcome has a probability of 1/4 – which is nothing interesting. However, if you make the inputs identical in every imaginable way, Fig 1.3(b) shows that you now only have three distinct possibilities. Either you get both inputs in one output or the other, or you get one in each output. Then, the probabilities are $\frac{1}{4}$, $\frac{1}{4}$, and $\frac{1}{2}$, respectively. Now these are still classical probabilities, so we the outcomes cannot *interact* with each other. In a quantum-mechanical system, you have complex probability amplitudes as discussed in 1.1.2. These probability amplitudes c_i add together to produce the output state, each having their own complex phase. Thus you can have a situation like 1.3(c) with the probability amplitude of observing one in each output *vanishing*, making this situation have zero probability and thus you can only ever observe the outputs coming out together from one port. This phenomenon is called the Hong-Ou-Mandel effect [4].

Now if we measure the outputs of the beamsplitter in the indistinguishable photon case, we will observe the state $|\psi_{\text{out}}\rangle = \frac{1}{\sqrt{2}}(|2\rangle_{\text{top}}|0\rangle_{\text{bottom}} + |0\rangle_{\text{top}}|2\rangle_{\text{bottom}})$. This state is a *superposition* state, which makes it a quantum system with no classical analog. There is a $(\frac{1}{\sqrt{2}})^2 = \frac{1}{2}$ probability that the photons will exit the top port as well as the bottom, but the photons are not definitely in *either* port until we measure them. This superposition is not merely a lack of knowledge on our part; it is a statement about the *physical inability to know* the definite state of the photons. Moreover, this state is not just a superposition state; it is an *entangled* state. Because the photons could be in either port, but we cannot know which until we measure it, we cannot write the state in the form $|\psi_{\text{out}}\rangle = |\psi\rangle_{\text{top}}|\psi\rangle_{\text{bottom}}$ (a product state) and thus the top and bottom modes are entangled by definition. Upon measurement of the top port we can immediately know the state of the bottom port, and vice-versa. This is another way in which quantum states can encode more information than classical states.

We now have all the elements we need to introduce the idea of using quantum optics to perform measurements – quantum metrology.
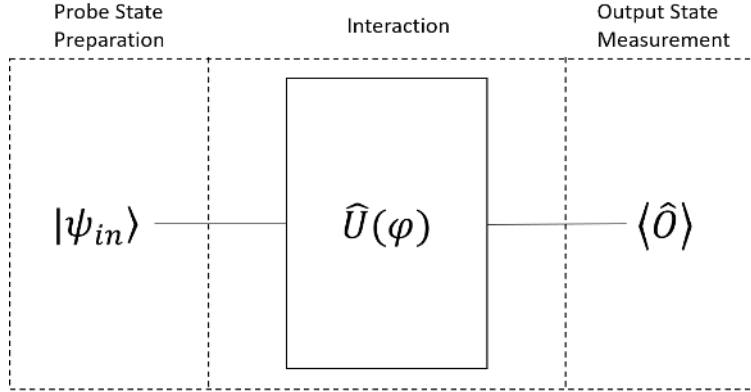
Figure 1.4. The generic phase-estimation problem diagram.

1.2 Quantum Metrology

Quantum metrology, and particularly phase-estimation, consists of three distinct components (as shown in Fig 1.4): probe state $|\psi_{\text{in}}\rangle$, unitary evolution $\hat{U}$, and output measurement $\hat{O}$. The end goal of any metrology system is, intuitively, to perform as precise of a physical observation as possible. There is some unknown quantity ϕ we want to know the value of, and we must choose our measurement apparatus carefully in order to extract the maximum amount of information about that quantity as possible.

We have discussed various states of light (both quantum and classical) in Sec. 1.1.1 – these will be utilized as *probe states* for metrology purposes. Given their unique statistical properties discussed in Sec. 1.1.2, the generic metrology scheme can utilize many different probe states. Typically, the decision of which probe state to use to perform the measurement depends on ease of preparation (thermal states, for example, are much simpler to prepare than single photons) as well as the statistics of the light, which typically favors sub-Poissonian states such as the two-mode squeezed vacuum state.

Once a probe state is chosen, we must use it to extract information about ϕ, the quantity of interest. This is where the unitary evolution $\hat{U}(\phi)$ comes in. A proper choice of $\hat{U}$ can cause the probe state to interact with ϕ strongly, resulting in an output state $|\psi_{\text{out}}(\phi)\rangle$ that contains a great deal of information about the unknown quantity. After imparting the phase-information into the probe state, all one must do is perform a measurement at the

output.

$$\hat{U}(\phi)|\psi_{\text{probe}}\rangle = |\psi_{\text{probe}}(\phi)\rangle. \tag{1.10}$$

A generic measurement is represented in quantum mechanics as a positive-operator valued measure (POVM). A quantity that represents a physical observable is written as the operator $\hat{O}$, and taking the expectation value of $\hat{O}$ with the output (evolved) state yields the real expectation value λ.

$$\langle\hat{O}\rangle = \langle\psi_{\text{probe}}(\phi)|\hat{O}|\psi_{\text{probe}}(\phi)\rangle = \lambda(\phi). \tag{1.11}$$

Since λ is an expectation value, it has a distribution parameterized by ϕ. The variance in λ is given by

$$\Delta\lambda = \sqrt{\langle\hat{O}^2\rangle - \langle\hat{O}\rangle^2} \tag{1.12}$$

If we are interested in performing a phase-estimation measurement, the quantity of interest is $\lambda(\phi) = \phi$ and $\Delta\lambda = \Delta\phi$. This quantity is called the phase uncertainty, and is bounded by the Heisenberg uncertainty principle

$$\Delta\phi \geq \frac{1}{\Delta n}, \tag{1.13}$$

where Δn is the variance or uncertainty in the photon number of the state that interrogates the phase.
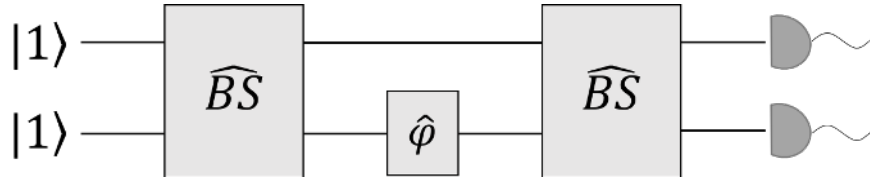
Figure 1.5. The Mach-Zehnder inteferometer.

As an example, consider the Mach-Zehnder interferometer (MZI) shown in Fig. 1.5.

With the input state $|\psi_{\text{in}}\rangle = |1\rangle|1\rangle$, we can calculate the output state of the MZI as

$$
\begin{aligned}
|\psi_{\text{out}}\rangle &= (\hat{BS})(\hat{\phi})(\hat{BS})|1\rangle|1\rangle \\
&= \frac{1}{\sqrt{2}}\sin{(\phi)}[|2\rangle|0\rangle - |0\rangle|2\rangle] - \cos{(\phi)}|1\rangle|1\rangle.
\end{aligned}
\tag{1.14}
$$

Then the associated probabilities are

$$
\begin{aligned}
P_{2,0} &= \frac{1}{2}\sin\phi^2, \\
P_{1,1} &= \cos\phi^2, \\
P_{0,2} &= \frac{1}{2}\sin\phi^2.
\end{aligned}
\tag{1.15}
$$

We can use any of these quantities as an estimator for ϕ, but it turns out that $P_{1,1}$ contains the *most* information about ϕ. For any observable with POVM $\hat{O}$, error-propagation gives us

$$
\Delta\phi = \frac{\sqrt{\langle\hat{O}^2\rangle - \langle\hat{O}\rangle^2}}{|\frac{d\langle O\rangle}{d\phi}|}
\tag{1.16}
$$

Using $|1,1\rangle\langle 1,1| = \hat{P}_{1,1}$ as our POVM, this corresponds to estimating the quantity $P_{1,1}$ as the MZI is performed multiple times. Then, with $\langle\hat{P}_{1,1}\rangle = P_{1,1}$ we can find the phase sensitivity of this scheme as

$$
\begin{aligned}
\Delta\phi &= \frac{\sqrt{\langle\psi_{out}|(|1,1\rangle\langle 1,1|)^2|\psi_{out}\rangle - (P_{1,1})^2}}{|\frac{d(P_{1,1})}{d\phi}|}, \\
&= \frac{\sqrt{\cos\phi^2 - \cos\phi^4}}{|2\cos\phi\sin\phi|}, \\
&= \frac{1}{2}.
\end{aligned}
\tag{1.17}
$$

It turns out that $\Delta\phi = 1/2$ is the *optimum* phase-sensitivity for the MZI with any input state of average photon number $\bar{n} = 2$. The twin single-photon input meets the *Heisenberg-limit* (HL – Eq. 1.18) in phase sensitivity,

$$\Delta\phi_{\text{HL}} \geq \frac{1}{N}, \tag{1.18}$$

where N is the average photon-number of the probe state. This quantity is in contrast to the classically-optimal phase sensitivity, the shot-noise limit (SNL) where $\Delta\phi_{\text{SNL}} \geq \frac{1}{\sqrt{N}}$. This disparity between the SNL and the HL is one of the primary indications of the true "superiority" of quantum metrology. Per given resource (here, photons), quantum mechanics shows us that we can gain much more information from a probed system than classical schemes can achieve.

We can prove that choosing $P_{1,1}$ as a witness to ϕ provides maximal information extraction from the evolved probe state, using the concept of the quantum Fisher information. One could rightly ask how we know if a given choice measurement is a good one, or rather if it extracts the maximal amount of information from the state. The quantum Fisher information (QFI), given by Eq. 1.19 relates the evolved probe state to the amount of phase information encoded in that state, *regardless of choice of measurement* [5],

$$F_Q(|\psi(\phi)\rangle) = 4(\langle\dot{\psi}(\phi)|\dot{\psi}(\phi)\rangle - |\langle\dot{\psi}(\phi)|\psi(\phi)\rangle|^2). \tag{1.19}$$

Note that Eq. 1.19 holds only for pure states, and that $|\dot{\psi}(\phi)\rangle = \frac{d|\psi(\phi)\rangle}{d\phi}$. Now, the Quantum Cramér-Rau Bound (QCRB) provides a simple relationship between the minimum phase uncertainty $\Delta\phi$ and the QFI [6],

$$\Delta\phi \geq \frac{1}{\sqrt{F_Q}}. \tag{1.20}$$

Plugging in Eq. 1.14 to the QFI, we get $F_{Q,\text{MZI}} = 4(1 - |0|^2) = 4$, and thus the minimum phase uncertainty for the phase estimation with an MZI is $\Delta\phi \geq \frac{1}{2}$ as previously obtained using the POVM $|1,1\rangle\langle1,1|$ as a witness to ϕ. This bound confirms that our choice of probe state, as well as the evolution of the state and performed measurement POVM saturate the QCRB and achieve optimal sensitivity. Note however that achieving the QCRB does *not*

guarantee that the optimal scheme is unique, only that we have discovered one such scheme.

Using the QFI, we can determine the optimality of any quantum metrology system. We can measure the phase-estimation performance against standard limits such as the SNL and HL to determine whether quantum phenomena are contributing enhanced precision, leading to a more resource-conscious measurement that out performs classical capabilities.

2 Sub-Shot-noise Metrology in Boson-Samplers

2.1 Motivation and Background

In this chapter I discuss the application of quantum metrology, particularly phase-estimation, to the topic of Boson-Sampling. This chapter is based heavily upon the collaborative efforts of the Quantum Science and Technologies group at Louisiana State University alongside the Department of Physics and Astronomy at Macquarie University in Sydney as well as the Centre for Quantum Photonics at the University of Bristol, UK. This work culminated in the publication given by Ref. [7]. The initial goal was to explore the quantum complexity of the Boson-Sampling device, and to see if its unique properties could lead to enhanced (below shot-noise) precision in phase-estimation. This current work was a followup to the initial work [8]; the specific goal of this work was to optimize the scheme for determining its absolute performance, as well as developing a more natural way of counting the relevant resources exploited. The results show a quantum-enhanced sensitivity that unfortunately dissipates as the device scales. However, the theoretical insight gained from the work in this dissertation is instrumental in followup works [9].

This chapter is organized as follows: First, in Sec. 2.2, I describe the general architecture, and compute the quantum Fisher information and quantum Cramér-Rao bounds. Second, in Sec. 2.3, I investigate the options for measurement interferometer in reference to the state preparation interferometer. In this section I also discuss various phase strategies for $\hat{\Phi}$ and find the optimal phase strategy. Third, in Sec. 2.4, I describe how different choices of $\hat{V}_1$ and $\hat{V}_2$ affect device sensitivity and find their optimal structure. Finally, in Sec. 2.5, I investigate how loss and dephasing errors affect the device performance.

A large fraction of the efforts of theoretical computing science and physics is now spent in the discovery of post-classical devices to display quantum supremacy. Much still remains a mystery about the limits and complexity of quantum computing. One well-studied example

---

of a device, which demonstrates a quantum advantage over its classical counterpart, came about as a result of discovering the Hong-Ou-Mandel effect, enabling interferometric sensors to estimate unknown variables with increased sensitivity [4]. It was then shown that bosonic NOON states would achieve asymptotically better sensitivities when compared to a comparable device using only classically-limited techniques, with an increasingly large number of probe photons N [10]. Like the elusive universal quantum computer, however, at present the experimental overhead for preparing NOON states is prohibitive, making practical applications infeasible [11, 12]. Although much is now understood about metrology in regards to two-mode interferometers, much less is known about multi-mode networks [5].

With the recemt advent of quantum-enhanced devices, like a boson sampler [13, 14], new attention has been drawn to the capabilities of more practical passive linear-optical networks. These systems create complicated number-mode entanglement with an exponentially large state space. If such an optical network is supplied with uncorrelated single photons, the output probabilities in the Fock basis are computed from complex matrix permanents, which are known to be #P-hard to compute exactly, and strongly believed to be computationally unrealistic quantities to estimate accurately [15, 16]. Already, BosonSampling has attracted much experimental interest as a simple approach for performing the first truly post-classical computation [17–21].

Recently the sensitivity of a passive linear optics setup, which consists of single photons passed into a specific multi-mode interferometer and photodetection at the output, was investigated [8, 22]. In this chapter, I study a significantly larger class of devices and further show that the sensitivity can be maximized in this system given realistic constraints with regard to the unknown phase. I show that the device reaching this optimality is not only significantly more sensitive than the one proposed in Ref. [8], but also far simpler to construct. I achieve this by using the Fisher information (FI) formalism as introduced in Ch. 1, which yields insight into the role of the different components of the interferometer and aids an explicit computation of the phase sensitivity for the optimal network—a result that was only

postulated in Ref. [8]. Additionally, I provide an exact analytic calculation for the phase sensitivity of the optimized network from matrix permanents, which is an improvement over the conjectured result of Ref. [8]. The primary result is that for $n < 7$ photons the system achieves sub-shot-noise limited phase sensitivity with a passive multi-mode linear-optical device using $O(n)$ optical elements. I believe that this work is experimentally within reach with the current infrastructure from Ref. [21].

Although previous models for sensitive quantum devices have shown better theoretical scaling in the as-of-yet unrealistic limit of large average photon number, many of these systems are limited to a more pessimistic scalability from an experimental perspective. These devices are generally not robust enough when noise models are employed, require nonlinear components, have an oppressive overhead in state preparation, or employ measurements that are difficult to implement [26,30]. For instance, an MZI with a TMSV input and parity detection performs extremely precise measurements in the noiseless regime, but the performance deteriorates quickly under dephasing and loss and requires high-efficiency number-resolving detectors with ranges that must scale with the average photon number [35].

2.2 QuFTI Schematic and Quantum Fisher Information

I first consider the Quantum Fourier Transform Interferometer (QuFTI) system, as shown in Fig. 2.1, developed by Motes, Olson, Rabeaux, Dowling, Olson and Rohde (MORDOR). As I described the generic phase-estimation problem in Ch. 1, the QuFTI consists of three critical components: first, a multi-mode input probe state $|\psi_{\text{in}}\rangle = |1\rangle^{\otimes n}$ of n single photons; next, an n-mode interferometer with a evolution matrix V_1 that performs the operation $\hat{V}_1$, followed by a generalized linear phase evolution $\hat{\Phi}$ which encodes the unknown phase to be estimated φ, and a second interference with a transfer matrix V_2 (enacting the transformation $\hat{V}_2$); lastly, coincidence photon detection at the exit ports. Let the phase-evolved probe be defined as $\hat{\Phi}\hat{V}_1|\psi_{\text{in}}\rangle \equiv |\psi_\varphi\rangle$ where $\hat{\Phi} = \exp\left(i\sum_j \hat{n}_j f_j \cdot \varphi\right)$, and $\hat{n}_i$ being the number operator for mode i. Then I define the measurement to be a second evolution with the transfer matrix V_2 followed by an array of "bucket" (non-number-resolving) photodetectors

17

(see Fig. 2.1) [8]. The most compelling aspect of the MORDOR design is that it is composed of single-photon input states, passive linear optics, and bucket detection, all of which can be implemented into an integrated photonic chip [23]. These simplifications bypass many of the technical challenges required to create NOON states [12], and the scheme is experimentally scalable with common equipment, though sub-shotnoise sensitivity is observed for only a small number of modes.

The interferometers $\hat{V}_1$, $\hat{V}_2$, and $\hat{\Phi}$ can be altered without jeopardizing the scalability of the device (see Fig. 2.1). Hence, a natural question arises: what are the optimal choices of $\hat{V}_1$, $\hat{V}_2$ and $\hat{\Phi}$ that yield maximum phase sensitivity? In this work I answer this question.
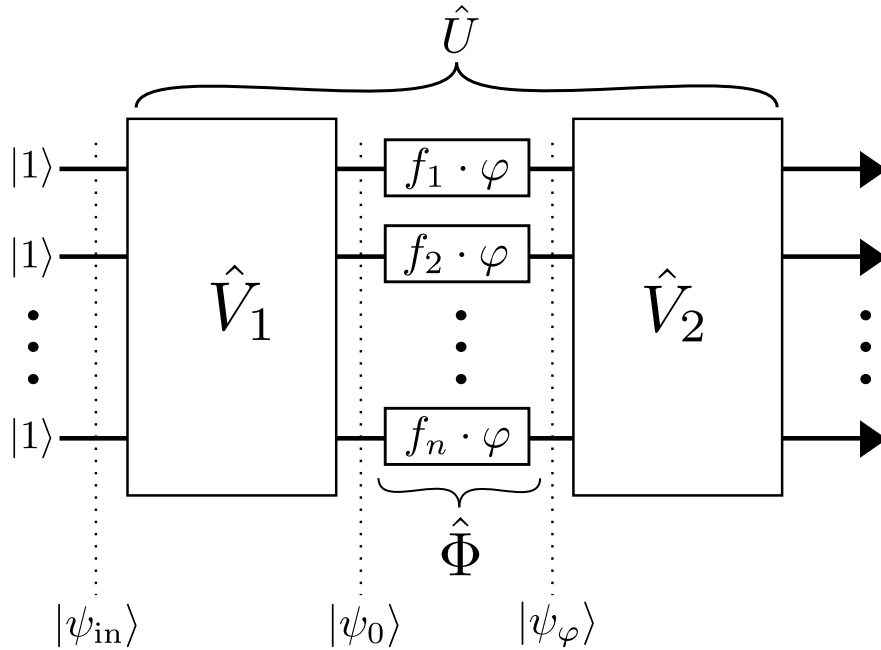
Figure 2.1. A generalized architecture for the quantum Fourier transform interferometer. I consider optimizations over $V_1, V_2 \in \mathrm{SU}(n)$ and phase strategies $\hat{\Phi}$, together with single photon inputs and photodetection in each mode. The MORDOR architecture can be restored when $V_2 = V_1^\dagger$, where V_1 is the n-mode Quantum Fourier Transform (QFT) and $f_j = (j-1)$ with j being the mode number.

To evaluate the phase sensitivity of different architectures, I utilize the quantum Fisher information (QFI) formalism, as discussed in Ch 1. Recall that (QCRB) [6],

$$\mathcal{F}(\rho_\varphi) \geq 1/(\Delta^2 \varphi), \tag{2.1}$$

18

where $\Delta^2\varphi$ is the variance in the estimate of φ. The QCRB can be saturated when one measures many instances of ρ_φ using an optimal basis [24]. Thus, the QFI is a useful way to quantify the information encoded into an evolved probe state related to an unknown parameter ϕ.

2.3 Phase Strategies

I evaluate the QuFTI scheme by investigating the role of $\hat{V}_2$. Note that measuring $|\psi_\varphi\rangle = \hat{\Phi}\hat{V}_1|\psi_{\text{in}}\rangle$ by sending it through the inverse operation $\hat{V}_2 = \hat{V}_1^\dagger$ then detecting it using single-photon detectors is an optimal measurement strategy around $\varphi = 0$. This measurement scheme projects $|\psi_\varphi\rangle$ onto the basis containing $|\psi_{\varphi=0}\rangle$. Projecting onto this basis has been shown to be an optimal measurement in Ref. [24]. To observe this more directly, I can compute the probability P for the observable event $\hat{O} = (|1\rangle\langle 1|)^{\otimes n}$ of detecting a photon at each output of the full interferometer $\hat{V}_2\hat{\Phi}\hat{V}_1$ to be $P = 1 - \varphi^2\mathcal{F}(|\psi_\varphi\rangle)/4 + \mathcal{O}(\varphi^4)$ when $\hat{V}_2 = \hat{V}_1^\dagger$, as shown in Appendix A.1. This allows us to compute the phase sensitivity $\Delta\varphi$ obtained from the error propagation formula in terms of QFI,

$$
\begin{aligned}
\Delta\varphi &= \frac{\sqrt{\langle\hat{O}^2\rangle - \langle\hat{O}\rangle^2}}{|\frac{d\langle\hat{O}\rangle}{d\varphi}|} \\
&= 1/\sqrt{\mathcal{F}(|\psi_\varphi\rangle)} + \mathcal{O}(\varphi^2).
\end{aligned}
\tag{2.2}
$$

Thus, when φ is very near 0, the QCRB is saturated by the error propagation formula, and hence, the choice of $\hat{V}_2 = \hat{V}_1^\dagger$ as the measurement is shown to be optimal; this is one of the primary results of this chapter. Note that the problem of minimizing the phase uncertainty of the system is equivalent to maximizing $\mathcal{F}(|\psi_\varphi\rangle)$ when $\hat{V}_2 = \hat{V}_1^\dagger$, as the precision computed by error propagation can be obtained by calculating the QFI, .

I turn now to the various candidates for f_i's, which is the phase strategy of choice as shown in Fig. 2.1. By interrogating an unknown phase shift with a probe state k times, the effect of the phase shift is amplified [25]. If the overall phase shift $k\theta$ applied to a mode can be determined within a given precision $\Delta^2(k\theta) = \alpha$, then the precision to which θ is

measured is increased by a factor of k^2, so that $\Delta^2\theta = \alpha/k^2$. This effect can be exploited to increase the precision of any measurement procedure, including those using exclusively classical techniques. Therefore, a fair comparison of different quantum strategies requires that I impose the normalization condition,

$$\sum_i f_i = 1, \tag{2.3}$$

i.e., I assume they all utilize the same total accumulated phase. Now I show that, given this normalization condition, the highest QFI can be achieved using a single phase strategy, i.e. $f_j = \delta_{j,1}$. Analogous to the MORDOR framework, the unknown phase is encoded by the unitary, $\hat{\Phi} = \exp\left(i \sum_j \hat{n}_j f_j \cdot \varphi\right)$. It follows that,

$$\begin{aligned}
\frac{1}{4}\mathcal{F}(|\psi_\varphi\rangle) &= \sum_{j,k} f_j f_k \operatorname{Cov}_0(\hat{n}_j, \hat{n}_k) \\
&\leq \sum_{j,k} f_j f_k \operatorname{Var}_0(\hat{n}_h) \\
&= \operatorname{Var}_0(\hat{n}_h),
\end{aligned} \tag{2.4}$$

where the covariance is $\operatorname{Cov}_0(A, B) \equiv \langle AB \rangle_0 - \langle A \rangle_0 \langle B \rangle_0$, for commuting operators A, B and mode h is understood to be the one with the largest photon number variance. If the phase shift was put only in mode h, then the QFI would simply be $4\operatorname{Var}(\hat{n}_h)$. I conclude that the distribution of phase shift between two or more modes leads to a QFI that is less than or equal to the QFI obtained when the phase shift is only in mode h. If I assume that the variance is largest in mode 1, which can be ensured by the choice of $\hat{V}_1$, the optimal phase distribution is $f_j = \delta_{j,1}$.

To illustrate the performance of different phase strategies, I consider a range of functions representing trial strategies (Table 2.1). For each phase strategy, I can use the result of Ref. [15] to numerically compute the phase sensitivity $\Delta\varphi$ using matrix permanents of $V_1\Phi V_1^\dagger$. This technique is summarized in Appendix A.2, and the result is plotted in Fig. 2.2. From

Sub-linear	$f_j^{\text{sub}} = \sqrt{j}$
Linear	$f_j^{\text{lin}} = j - 1$
Quadratic	$f_j^{\text{quad}} = j^2$
Exponential	$f_j^{\text{exp}} = 2^j$
Delta	$f_j^{\delta} = \delta_{j,1}$

Table 2.1. Functions representing the trial phase strategies. Note that many of the strategies are unnormalized and do not satisfy Eq. (2.3), but can easily be made so by dividing each by $\sum_{j=1}^{n} f_j$.

this figure, it is clear that no improvement is made in phase sensitivity by distributing the phase over the modes, and restricting φ to only one mode is most effective. This result is consistent with the results of Berry *et al.* as shown in Ref. [27].
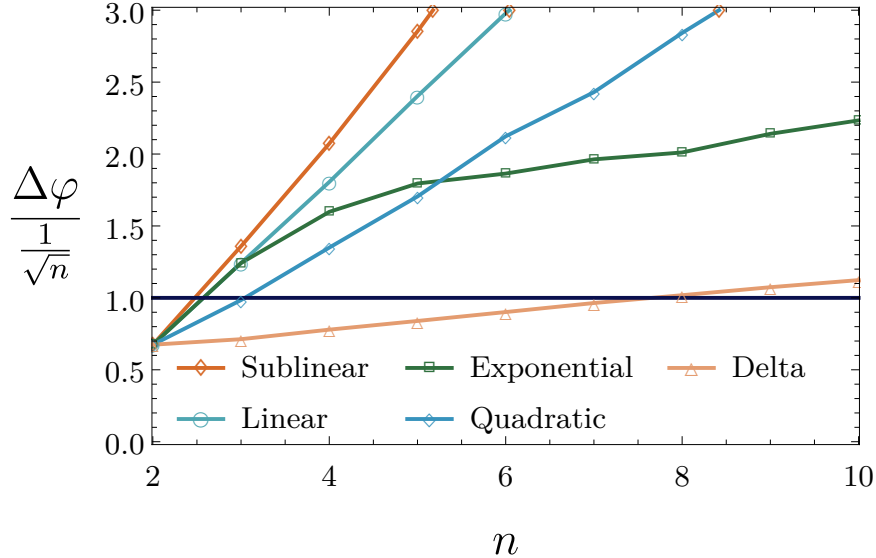
Figure 2.2. The phase sensitivity scaling of differing phase strategies for the QuFTI suggests that increasing the "phase gap" between modes increases the phase sensitivity. The shot-noise limit used for comparison is here defined to be $1/\sqrt{n}$, which is the optimal classical scheme for n photons and number of modes greater than two. The region where the phase sensitivity falls below one indicates super-sensitivity. It is apparent that the delta phase strategy is optimal.

With this in mind, I would like to now compare the architecture described in the original MORDOR work to the new phase strategy described above that optimizes the QuFTI. However, I have already made this comparison, since MORDOR possesses the linear phase strategy $f_j = j - 1$, whose normalized strategy is plotted against the optimal strategy in

Fig. 2.2. This is contradictory to the preliminary results in MORDOR, which showed that for all n, the phase sensitivity of MORDOR beats the shotnoise limit. This is because MORDOR used a different resource counting technique called *ordinal resource counting* (ORC). The ORC strategy found in MORDOR did not obey the normalization condition on the phase shifts that I have imposed here in Eq. (2.3). For that reason, the comparison in MORDOR with the classical strategy chosen to represent the shot-noise limit was unfair. The subsequent errata of Ref. [8] is indeed consistent with the normalized result here. Thus, when the normalization condition of Eq. (2.3) is imposed, the linear phase strategy used in MORDOR is sub-optimal.

In Fig. 2.4 I show the phase sensitivity of the QuFTI with the delta phase strategy and compare it to the SNL and the HL. I see that I do better than shot-noise for $n \leq 6$ photons, which is well above what is experimentally achievable today, suggesting that this type of quantum metrology might be the best route forward in the medium-term.

Figure 2.3. Phase sensitivity of the optimal QuFTI, which consists of the delta phase strategy for $\hat{\Phi}$, $\hat{V}_2 = \hat{V}_1^\dagger$, where $\hat{V}_1$ is the n-mode Quantum Fourier Transform (QFT), compared to the shot-noise limit and the Heisenberg limit.
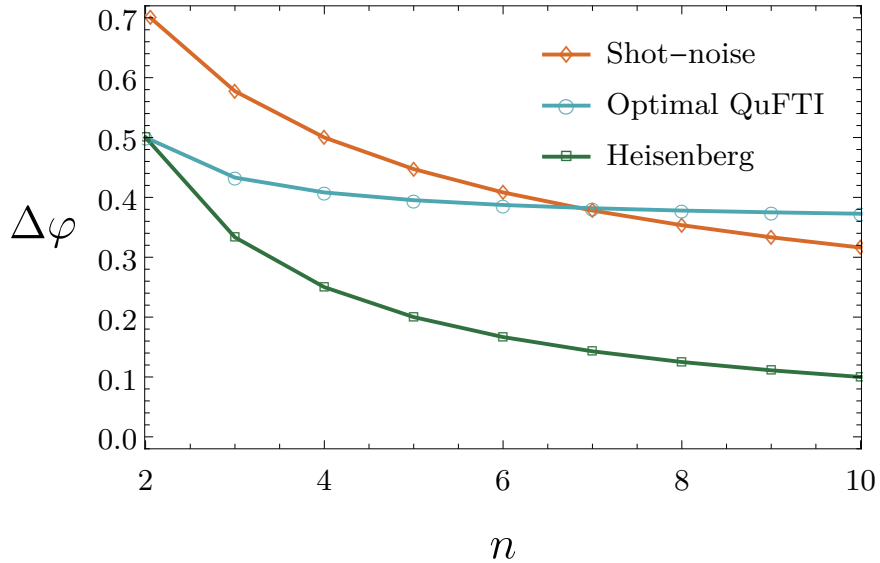
2.4 Results

In this section, I investigate the effect that $\hat{V}_1$ has on the phase sensitivity, when using the previously found optimal components $\hat{V}_2 = \hat{V}_1^\dagger$ and $f_i = \delta_{1,i}$, the best phase strategy. In Sec. 2.3 it was shown that when the phase shift is placed in the first mode i.e. $f_i = \delta_{1,i}$, then $\mathcal{F}(|\psi_\varphi\rangle) = 4 \cdot \text{Var}_0(\hat{n}_1)$. For an input state of single photons $|1\rangle^{\otimes n}$ fed into $\hat{V}_1$, I can explicitly compute, as shown in Appendix A.3, that $\mathcal{F}(|\psi_\varphi\rangle) = 8\left(1 - \sum_{i=1}^{n} |V_{1,i}|^4\right)$, where $V_{1,i}$ is the ith element in the top row of V_1. Physically, this means the Fisher information is dependent only on the coupling between the input modes and and the first output mode. This is perhaps intuitive, since only the first mode interrogates the phase. Additionally, I can compute the QFI when k photons $|k\rangle^{\otimes n}$ are fed into each mode of $\hat{V}_1$ to be,

$$\mathcal{F}(|\psi_\varphi\rangle) = 4\left(1 - \sum_{i=1}^{n} |V_{1,i}|^4\right) k(k+1), \tag{2.5}$$

which is maximized for V_1 with $|V_{1,i}| = 1/\sqrt{n}$ for all top row elements. Note that while the QuFTI satisfies this constraint, it does not do so uniquely. To be as general as possible, then, I consider any unitary with this structure to be "uniform" and any interferometer with these unitaries to be a Quantum Uniform Multi-mode Interferometer (QUMI). A QuFTI is thus a special case of a QUMI. Most remarkably, because the phase sensitivity of the scheme relies only on the values of the top row of the matrix V_1, a network can achieve the maximum sensitivity with only $O(n)$ beamsplitters—this is a great improvement over the MORDOR architecture's QuFTI, which requires $O(n^2)$ beamsplitters to implement. A simple implementation of this new architecture is displayed in Fig. 2.4, where the reflectivity amplitude of the beamsplitter acting on modes 1 and k should be $1/\sqrt{k}$. Setting $|V_{1,i}| = 1/\sqrt{n}$ gives,

$$\mathcal{F}_{\text{max}}(|\psi_\varphi\rangle) = 4k(k+1)\left(1 - 1/n\right). \tag{2.6}$$

This reduces to the results of Holland and Burnett when $n = 2$ modes [28]. In Ch. 3 I show how it is possible to make k-photon Fock input states starting with only single photons using more advanced devices, such as utilizing a reliable quantum memory, which is currently beyond experimental techniques.

For an input state of single photons, the optimal precision obtainable is

$$\Delta\varphi = 1/\sqrt{8(1 - 1/n)}. \tag{2.7}$$

One can also derive at the same result by an explicit computation of matrix permanents when $V = V_1 = V_2^\dagger$, which I provide in Appendix A.4.

To investigate the sensitivity of a device in which $\hat{V}_2 = \hat{V}_1^\dagger$ but wherein $\hat{V}_1$ is not optimal, I computed the phase sensitivity of 10,000 random unitary matrices in $\mathrm{SU}(n)$ (for each n), and plotted the optimal phase sensitivity (i.e. minimum $\Delta\varphi$) and average phase sensitivity of this set compared to the phase sensitivity of the optimal QUMI (see Fig. 2.5). It is now apparent that the best strategy is to use the delta phase function and the QUMI. I call this overall best strategy, which has the optimal delta phase shift, combined with the uniformly-weighted top row of the unitaries, the optimal QUMI. Note: although an experimental implementation of the QuFTI is not optimal for QUMIs, I use the QuFTI for analytic simulation and computation, since the matrix itself has many useful symmetries but still produces the same output statistics as any QUMI.

2.5 Experimental Errors

Quantum states such as single photons are known to be difficult to manipulate. It is then important to consider how various types of errors affect the quality of metrology protocols. In particular the loss and dephasing are considered. Particularly, such effects generate mixed states for which the QFI is quite difficult to calculate as noted in Ch. 1. In addition, the QFI is not practically informative if you cannot perform the optimal measurement due to
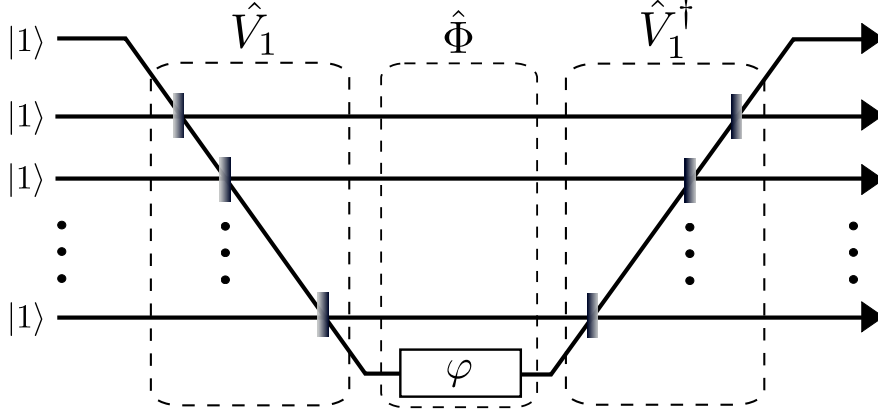
Figure 2.4. A simple architecture which maximizes the phase sensitivity of the scheme. The beamsplitters (grey boxes) should be adjusted so that V_1 is a QUMI, namely, the reflectivity amplitude of the beamsplitter acting on mode 1 and mode k should be $1/\sqrt{k}$.

engineering limitations.

For example, when simulated loss is applied to a quantum state, the optimal measurement strategy can require exotic techniques such as non-demolition measurement and feed-forward [30]. Therefore calculating the QFI is not always a good indicator of the performance of a practical strategy. Because of this issue, I study the performance of the system by directly calculating the phase sensitivity of specific measurement results from realistcally-implementable measurement techniques.

2.5.1 Loss Analysis

Loss is a significant issue to overcome in any experiment which utilizes single photons.

One hurdle when one considers photon loss in the device presented here is that, if the device relies solely on on-off photon detectors, a loss event is indistinguishable from that of a photon collision event. Hence, for small values of φ, it may be true that the loss dominates the number of perceived collisions and one is unable to extract any useful information about φ. Employing limited photo-resolution (i.e. detectors with the capability of distinguishing between states that have one photon from those that contain two or more) can partially solve this issue, though photon losses that correspond to one of the photons in a collision event will still degrade the signal. Of course, the advantage of being able to employ simple
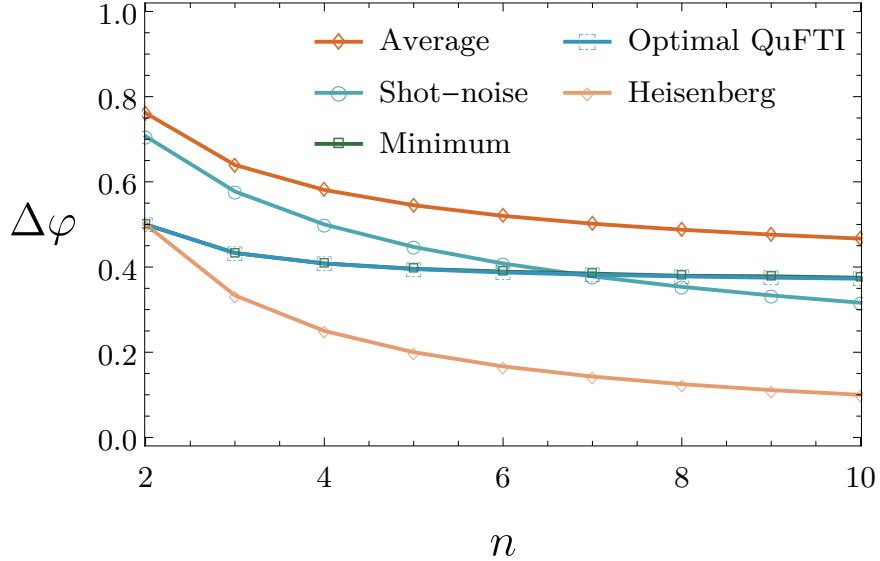
Figure 2.5. The Quantum Fourier Transform (QFT) is optimal for the delta phase strategy. However, it is not uniquely so – any uniform unitary is also optimal for this strategy.

photodetectors is then lost in the case that you retain the exact architecture previously presented. It is however possible to implement pseudo-number-resolving detection for small numbers of photons by simply coupling the output modes with additional vacuum modes via beamsplitters; the output of these extra modes then can use the simpler photodetector. Members of my team have also done an exhaustive calculation of loss in the context of BOSONSAMPLING in [32,33], where both effects of spatial and temporal losses are considered.

If enough is known about the noise profile beforehand, one can still extrapolate information about φ despite the noisy data. For example, if every individual photon has an independent and equal chance of being lost, then the sensitivity $\Delta\varphi$ degrades continuously according to the photon fidelity ℓ. Suppose $P(\varphi)$ corresponds to the probability of measuring the $|1\rangle^{\otimes n}$ outcome. If no photons or only a single photon is lost, the probability of detecting an unambiguous collision event is then

$$\Pr(\text{collision}) = (1 - P)[\ell^n + (n - 2)(1 - \ell)\ell^{n-1}]. \tag{2.8}$$

This can then be plugged in to the error propagation formula of Eq. (2.2) to give the sensi-

tivity $\Delta\varphi$ (see Fig. 2.6).
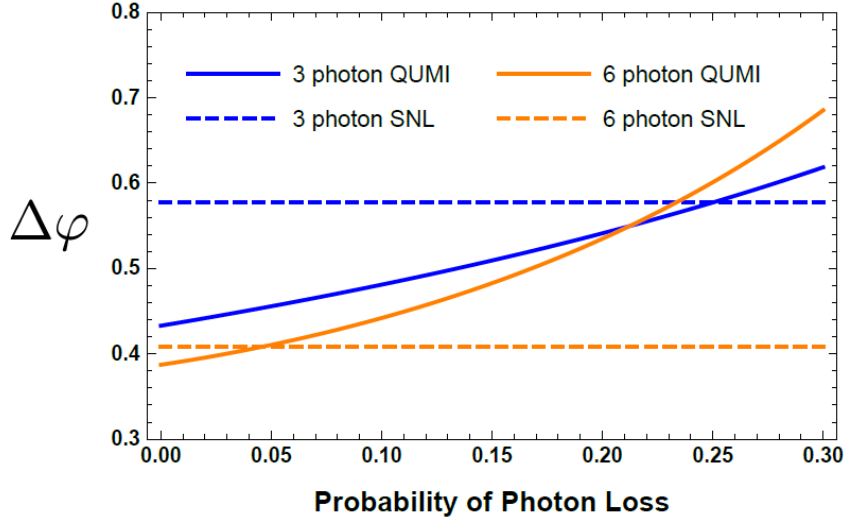
Figure 2.6. Sensitivity of lossy 3- and 6-photon QUMIs (solid lines) compared to their respective shotnoise limits (dashed lines) at $\varphi = 0.001$. The probability on the x-axis corresponds to the loss rate for each photon independently in the device.

Recent experimental accomplishments have demonstrated that linear optical networks, particularly for systems of the size considered here, can be constructed with very low loss. Networks (with more modes and optical elements than I consider here) have been demonstrated with up to 99% efficiency [37]; additionally, single photon detectors have achieved up to 93% efficiency [38]. Given the rapid advances in experimentally constructing optical networks, photon loss may soon be a source of error that is negligible for the devices considered in this chapter.

2.5.2 Dephasing Analysis for the Optimal QuFTI

Another type of error that often presents itself in optical networks is dephasing. Here I will analyze dephasing in the optimal QuFTI architecture and compare them to NOON states in a standard Mach-Zehnder interferometer.

Dephasing with only a single phase shift is modeled with dephasing only occurring in the mode with the unknown phase. In the rest of the architecture, dephasing can be made
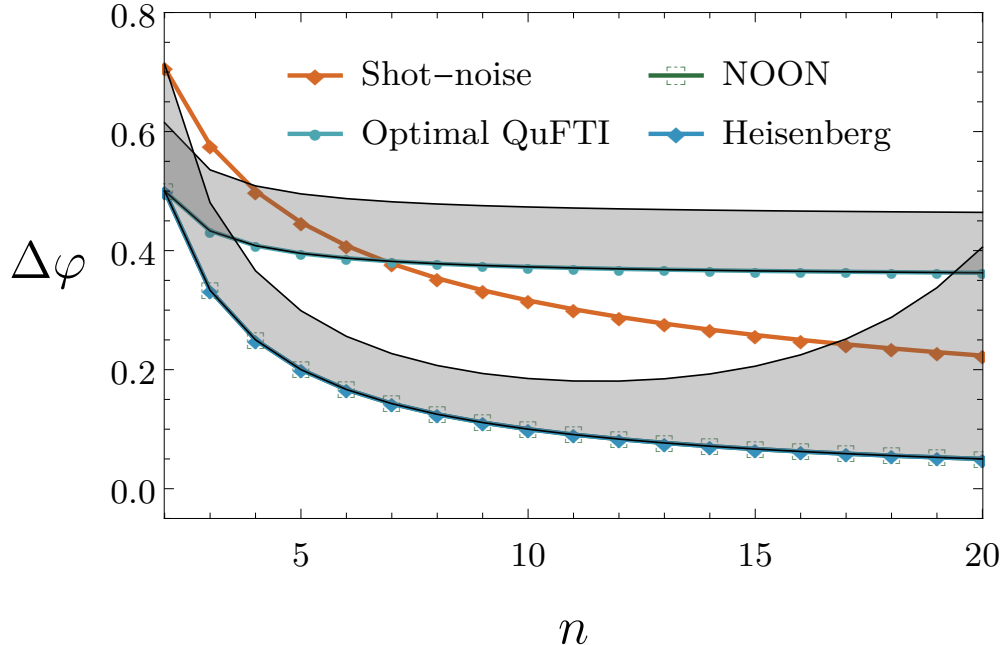
Figure 2.7. Dephasing with the optimal QuFTI for $\varphi = 0.1$. This is compared to the shot-noise limit, the Heisenberg limit, and the NOON state with dephasing [34]. The shaded regions denote the dephasing regime of $0 \leq \Delta\chi \leq 0.005$ for both the optimal QuFTI and NOON states.

very close to zero. I insert a random phase shift χ to the single mode, which is a Gaussian random variable of zero mean $\langle\chi\rangle = 0$ but nonzero second order moment $\langle\chi^2\rangle = \Delta\chi$,

$$e^{\pm i\varphi} \mapsto e^{\pm i(\varphi+\chi)}. \tag{2.9}$$

When both $\varphi, \chi \ll 1$, the approximate form of P derived in Appendix A.4 becomes,

$$P = 1 - \frac{2n-2}{n}(\varphi+\chi)^2 + O(\varphi^4), \tag{2.10}$$

and correspondingly,

$$\langle P \rangle \approx 1 - \frac{(2n-2)(\varphi^2+\Delta\chi)}{n}, \tag{2.11}$$

which is then substituted into Eq. (2.2) to derive the phase sensitivity. Using this result, I numerically plot the phase sensitivity with dephasing in Fig. 2.7 for $0 \leq \Delta\chi \leq 0.005$

and $\varphi = 0.1$. I see that, in the sub-shotnoise regime, the optimal QuFTI interferometer is comparable in dephasing with the NOON state in an MZI—another well-known metrological scheme.

It is important to note that when $\Delta\chi$ is close to or larger than the value of $\sqrt{\varphi}$, the estimator P is very poor because it is unable to differentiate between a positive or negative value of $(\varphi + \chi)$. Indeed, for $\varphi = 0, \Delta\chi \neq 0$, the formula in Eq. (2.2) does not converge since $\langle P \rangle_{\varphi=0} \neq 1$. One straightforward solution is to utilize a known, controlled additional phase to shift the average phase far enough away from the peak of P so that, combined with the noise, the phase is predominantly positive or negative.

2.6 Conclusion

In this chapter I have considered a variety of different phase and unitary strategies for implementing a passive, single-photon input multi-mode metrological scheme. I have shown that the optimal architecture for n single photons is a QUMI, which equally couples each mode to a single phase resource in one of the arms of the interferometer, followed by the inverse of the QUMI. For $n < 7$, the sensitivity of the optimal QUMI is sub-shotnoise. In the limit of n photons, the sensitivity tends towards a constant. This limit, however, assumes all photons are used in a single experiment. The scheme can always be made to beat the shotnoise limit asymptotically by choosing an architecture with $n < 7$ modes and repeating the experiment many times.

Perhaps the most appealing feature of the proposed device is that it can be implemented with only passive linear optics, single photon sources, and bucket detectors. In addition, it does not require any of the complicated phase arrangements from the scheme in Motes, Olson, Rabeaux, Dowling, Olson and Rohde. The technology to implement the optimal system is essentially that of BOSONSAMPLING, and is achievable in experimental setups that have already been implemented.

3 Fock-state Preparation Strategy

3.1 Motivation and Background

Fock states are a ubiquitous resource for many quantum technologies [39, 40], ranging from quantum communication and cryptography, to quantum-enhanced metrology [41–45], and optical quantum information processing [47]. There has been much progress made in single-photon preparation technology, creating large photon-number Fock states remains a challenge. Large Fock states are relatively easily prepared from single-photon states when utilizing non-deterministic linear optics, or by process of heralded spontaneous parametric down-conversion (SPDC). However, the scalability in preparing these states is a problem owing to inefficient (inverse exponential) scaling of the preparation probability versus the desired number of photons.

It is known that quantum-enhanced metrology reaches the HL when NOON states are used [10]. However, creating NOON states with large photon number carries difficult requirements similar to building a universal optical quantum computer, as it requires many of the same technologies such as a quantum memory, and use of fast feed-forward. Nevertheless, one requires Fock states with a large photon number to first create large NOON states for quantum-enhanced metrology [41]. Therefor, efficient schemes for creating Fock states with large photon-number, as presented in this chapter, are a crucial stepping stone for realizing optimal quantum-enhanced metrology.

Here, a bootstrapped protocol to iteratively building up large photon-number Fock states from the sole resource of single photons is presented and analyzed. It is shown that particularly the bootstrapped technique improves scalability exponentially compared to naïve single-shot preparation methods, yielding efficient (polynomial time) state preparation. Experimental requirements for this scheme are much the same as for universal linear optics quantum computing (LOQC) [47]. Although this is presently challenging, the state-construction

---

This bulk of the work in this chapter appeared previously as Ref. [29] published under Copyright © 2016 by the American Physical Society

method will be viable when all-optical quantum computing comes to bear.

This chapter is structured as follows. In Sec. 3.2, I discuss the most common form of Fock state preparation — heralded SPDC (as discussed in Ch. 1) — where detect some number of photons in one mode, guaranteeing an equal number of photons in the other. In Sec. 3.3, I present a naïve brute-force method to preparing large photon-number Fock states via post-selected linear optics — an inefficient technique, requiring exponential resources both in time and resource states. Then in Sec. 3.4, I present an improved technique, which is based on post-selected linear optics, wherein larger Fock states are built up progressively by combining smaller Fock states. Then I also introduce a recycling protocol, which improves exponentially the efficiency of state preparation when compared to the previously-described schemes. In Sec. 3.5, fusion is discussed; i.e. how does the choice of the order in which Fock states are fused affect resource scaling? Specifically, I describe the fusion protocol, discuss some analytic approximations, and speak about specific fusion strategies that are implemented. In Sec. 3.6 I discuss the converse protocol, where the goal is to reduce photon number, allowing reduction of a prepared Fock state with more than the desired photon-number to be shrunk to the target size. All of the results are presented in Sec. 3.7, where the different Fock state preparation algorithms are numerically simulated. In Sec. 3.8 I conclude this chapter and discuss future experimental implementation issues that require consideration, specifically those of inefficiencies and imperfect mode-overlap.

3.2 Spontaneous Parametric Down-Conversion

The most trivial approach to preparing large Fock states is to employ post-selected SPDC. Here, one exploits the photon-number correlations in the signal and idler modes of the TMSV state. Upon detecting n photons in one mode, it is guaranteed to having prepared exactly n identical photons in the other, assuming perfect detector efficiency, as shown in Fig. 3.1. Small Fock states of maximum size three photons have been prepared experimentally using this approach [48].

An SPDC source down-converts photons from a laser source with amplitude α into iden-
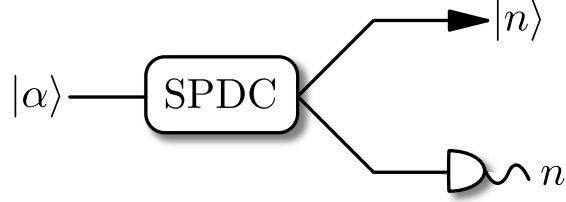
Figure 3.1. Conditional preparation of the n-photon Fock state through post-selected SPDC. A non-linear crystal is pumped by a coherent state $|\alpha\rangle$, yielding a TMSV state given by a highly-correlated superposition in the photon-number basis. Due to perfect photon-number correlations between the output modes, detection of n photons in the first output mode guarantees the preparation of n photons in the second. While in principle this works for arbitrary n, the probability of success decreases exponentially with n.

tical photon pairs across the two output modes via a second-order non-linear interaction. This evolution is given by the Hamiltonian

$$\hat{H}_{\text{SPDC}} = \chi \hat{a}_{\text{pump}} \hat{a}_{\text{signal}}^{\dagger} \hat{a}_{\text{idler}}^{\dagger} + \text{h.c.}, \tag{3.1}$$

where χ is the interaction strength, and depends on the non-linear material. This produces a TMSV state, which is a superposition in the photon-number basis,

$$|\psi_{\text{SPDC}}\rangle = \sum_{n=0}^{\infty} \lambda_n |n, n\rangle, \tag{3.2}$$

where the photon-number distribution is, as you may recall from Ch. 1, given by

$$|\lambda_n|^2 = \frac{1}{\bar{n} + 1} \left(\frac{\bar{n}}{\bar{n} + 1} \right)^n, \tag{3.3}$$

and $\bar{n}$ is the mean number of photons in the field, which is a function of the pump-power α. Evidently, there is a perfect photon-number correlation between the signal and idler output modes, yielding a direct approach to non-deterministic preparation of Fock states with arbitrary photon number. Suppose we wish to prepare a large photon-number Fock

state of at least d photons. The probability of successful preparation is then

$$P_{\text{prep}}(d) = \sum_{n=d}^{\infty} |\lambda_n|^2 = \left(\frac{\bar{n}}{\bar{n}+1}\right)^d,$$ (3.4)

which scales as inversely exponential in d, and therefore the average number of attempts required until success also scales exponentially with d. Further, in present-day laboratories, $\bar{n} \ll 1$ [49], causing this approach to be unrealistic for large d. In Fig. 3.2, the preparation probability for modest values of d is illustrated.
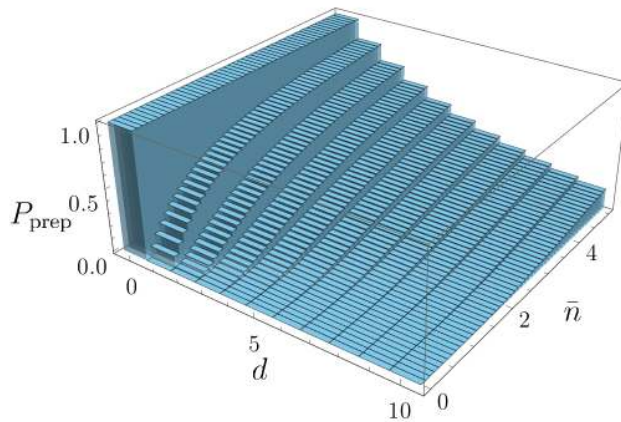
Figure 3.2. The probability of preparing a state of d photons or more in one mode of an SPDC source with mean photon number $\bar{n}$, by post-selecting the trials wherein one measures at least d photons in the other mode.

3.3 Single-shot Preparation

Utilizing only single-photon sources as a resource (from SPDC or other source technology), the obvious linear-optical way to prepare large Fock states is to simply input single-photon states into the input modes of the network, and post-select upon trials wherein one detects vacuum in all but one of the outputs. When this post-selection succeeds, the conservation of photon-number ensures that all photons output through the unmeasured mode. This concept is illustrated in Fig. 3.3.

Let us now consider an n-mode interferometer with only one photon at each input mode
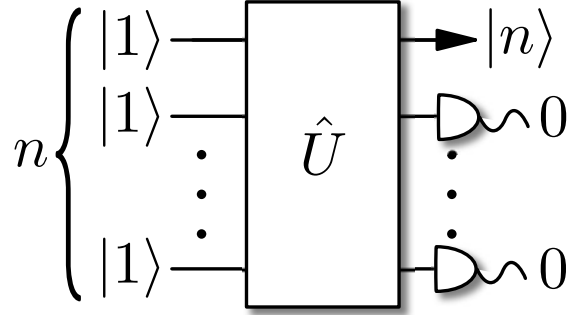
Figure 3.3. Single-shot preparation of an n-photon Fock state from n single input photons. A photon is incident upon each of the input modes, and we post-select upon detection of vacuum in all but one of the outputs, where all of the input photons must have exited in the remaining output mode.

as we did in Ch A. Then the input state has the form

$$|\psi_{\text{in}}\rangle = |1\rangle^{\otimes n} = \hat{a}_1^\dagger \ldots \hat{a}_n^\dagger |0\rangle^{\otimes n} = \left[\prod_{i=1}^n \hat{a}_i^\dagger\right] |0\rangle^{\otimes n}, \tag{3.5}$$

where $\hat{a}_i^\dagger$ is the creation operator for the ith mode, as discussed in Ch. 1.

Next, we apply a linear optical network, which implements the unitary map on the creation operators

$$\hat{U}\hat{a}_i^\dagger \hat{U}^\dagger \mapsto \sum_{j=1}^n U_{i,j}\hat{a}_j^\dagger, \tag{3.6}$$

which yields

$$\begin{aligned}|\psi_{\text{out}}\rangle &= \hat{U}|\psi_{\text{in}}\rangle \\ &= \left[\prod_{i=1}^n \sum_{j=1}^n U_{i,j}\hat{a}_j^\dagger\right]|0\rangle^{\otimes n}.\end{aligned} \tag{3.7}$$

Post-selecting upon every photon being output to the first mode (i.e. vacuum in all other

modes), the projected state is given by

$$
\begin{aligned}
|\psi_{\text{proj}}\rangle &= \left[\prod_{i=1}^{n} U_{i,1}\hat{a}_1^\dagger\right]|0\rangle^{\otimes n} \\
&= \sqrt{n!}\left[\prod_{i=1}^{n} U_{i,1}\right]|n\rangle|0\rangle^{\otimes n-1},
\end{aligned}
\tag{3.8}
$$

and thus the probability of this event occurring is

$$
P_{\text{bunch}} = n!\left|\prod_{i=1}^{n} U_{i,1}\right|^2.
\tag{3.9}
$$

In cases of a balanced interferometer like that of the QuFTI, we have

$$
|U_{i,1}| = \frac{1}{\sqrt{n}} \,\forall\, i,
\tag{3.10}
$$

and then

$$
P_{\text{bunch}} = n!\left|\prod_{i=1}^{n} \frac{1}{\sqrt{n}}\right|^2 = \frac{n!}{n^n} \sim \frac{\sqrt{n}}{e^n}.
\tag{3.11}
$$

Thus, the preparation probability for an n-photon Fock state again decreases exponentially in n. Thus, any realistic experimental implementation would necessarily be limited to relatively small values of n.

As a simple example, consider the two-photon HOM interference from Ch. 1. In this instance $n = 2$, and

$$
P_{\text{bunch}} = \frac{2!}{2^2} = \frac{1}{2},
\tag{3.12}
$$

as expected, because the output of a HOM interferometer is $|\psi_{\text{out}}\rangle = (|2,0\rangle + |0,2\rangle)/\sqrt{2}$.
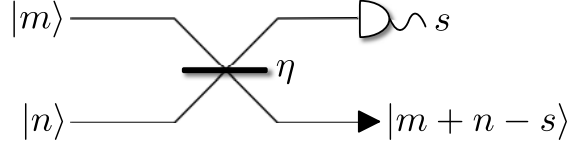
Figure 3.4. The Fock state fusion procedure. Two Fock states containing m and n photons are interfered on a beamsplitter with reflectivity η. Upon detection of s photons in the first output, an $m + n - s$ photon state is necessarily prepared in the other mode.

3.4 Bootstrapped Preparation

To improve upon the unfavorable scaling in the single-shot approach, consider a "bootstrapped" strategy where progressively larger Fock states are built using iterative application of a fusion procedure. The fusion device is simply a beamsplitter, with two Fock states input having with photon numbers m and n, and where one output mode is projected into the photon-number basis. If no photons are detected in the detected output mode, this yields a larger Fock state of size $m + n$ in the lower mode. When s photons are detected here, a subtracted state of size $m + n - s$ has been prepared, as shown in Fig. 3.4.

The state used as input to the fusion operation is given by

$$
\begin{aligned}
|\psi_{\text{in}}\rangle &= |m, n\rangle \\
&= \frac{1}{\sqrt{m!n!}} (\hat{a}^\dagger)^m (\hat{b}^\dagger)^n |0, 0\rangle,
\end{aligned}
\tag{3.13}
$$

which is then incident upon a beamsplitter of reflectivity η. We represent this evolution as

$$
U_{\text{BS}} = \begin{pmatrix} \eta & \sqrt{1 - \eta^2} \\ \sqrt{1 - \eta^2} & -\eta \end{pmatrix},
\tag{3.14}
$$

where local phases are, as usual, irrelevant. Then the output state is

$$
\begin{aligned}
|\psi_{\text{out}}\rangle &= \hat{U}_{\text{BS}}|\psi_{\text{in}}\rangle \\
&= \frac{1}{\sqrt{m!n!}}(\eta\hat{a}^\dagger + \sqrt{1-\eta^2}\hat{b}^\dagger)^m \\
&\quad \times (\sqrt{1-\eta^2}\hat{a}^\dagger - \eta\hat{b}^\dagger)^n|0,0\rangle \\
&= \frac{1}{\sqrt{m!n!}}\sum_{j=0}^{m}\binom{m}{j}\eta^j\sqrt{1-\eta^2}^{m-j}(\hat{a}^\dagger)^j(\hat{b}^\dagger)^{m-j} \\
&\quad \times \sum_{k=0}^{n}\binom{n}{k}\sqrt{1-\eta^2}^{k}\eta^{n-k}(-1)^{n-k} \\
&\quad \times (\hat{a}^\dagger)^k(\hat{b}^\dagger)^{n-k}|0,0\rangle \\
&= \frac{1}{\sqrt{m!n!}}\sum_{j=0}^{m}\sum_{k=0}^{n}\binom{m}{j}\binom{n}{k}\eta^{n+j-k}\sqrt{1-\eta^2}^{m+k-j} \\
&\quad \times (-1)^{n-k}(\hat{a}^\dagger)^{j+k}(\hat{b}^\dagger)^{m+n-j-k}|0,0\rangle \\
&= \frac{1}{\sqrt{m!n!}}\sum_{j=0}^{m}\sum_{k=0}^{n}\binom{m}{j}\binom{n}{k}\eta^{n+j-k}\sqrt{1-\eta^2}^{m+k-j} \\
&\quad \times (-1)^{n-k}\sqrt{(j+k)!(m+n-j-k)!} \\
&\quad \times |j+k, m+n-j-k\rangle.
\end{aligned}
\tag{3.15}
$$

Analyzing the case where s photons are measured in the first mode, an s-photon-subtracted state in the second mode is thereby produced. Thus, let $s = j + k$, and so the unnormalized (and post-selected) state reduces to

$$
\begin{aligned}
|\psi_{\text{ps}}\rangle &= \sqrt{\frac{s!(m+n-s)!}{m!n!}}\sum_{j=0}^{m}\binom{m}{j}\binom{n}{s-j}\eta^{n+2j-s} \\
&\quad \times \sqrt{1-\eta^2}^{m+s-2j}(-1)^{n-s+j}|s, m+n-s\rangle.
\end{aligned}
\tag{3.16}
$$

The probability of detecting s photons is then

$$P_{\text{sub}}(s|m,n) = \eta^{2(n-s)}(1-\eta^2)^{m+s}\frac{s!(m+n-s)!}{m!n!}$$
$$\times \left|\sum_{j=0}^{s}\binom{m}{j}\binom{n}{s-j}\left[\frac{\eta^2}{\eta^2-1}\right]^j\right|^2. \qquad (3.17)$$

The conditionally-prepared output state will have grown only if the s-photon-subtracted state is larger than both of the input states which have photon number m and n. Thus, we require $s < m+n - \max(m,n)$. Then the probability of preparing a state equal to or greater than both the input Fock states is

$$P_{\text{grow}}(m,n) = \sum_{s=0}^{m+n-\max(m,n)-1} P_{\text{sub}}(s|m,n). \qquad (3.18)$$

In the case of the unrecycled protocol, we only accept the $s = 0$ outcome, so the sum is eliminated and only the $s = 0$ term is kept.

The goal is to optimize this probability such that the likelihood of growing the state is maximized, so for each possible configuration of input Fock states m and n, we optimize η to maximize P_{grow},

$$\begin{aligned} P_{\text{opt}}(m,n) &= \max_{\eta}[P_{\text{grow}}(m,n)], \\ \eta_{\text{opt}}(m,n) &= \text{argmax}_{\eta}[P_{\text{grow}}(m,n)]. \end{aligned} \qquad (3.19)$$

3.5 Fusion Strategy

Figure 3.5 shows the optimal beamsplitter reflectivities and growth probabilities for $1 \leq m \leq 10$ and $1 \leq n \leq 10$. Evidently, when employing recycling (i.e. accepting all outcomes s) the growth probability is maximized when fusing two Fock states of equal photon number, $m = n$. This suggests that the optimal strategy for performing the fusion operations is to always fuse together states of equal size. This is analogous with the cluster state [50,51]

38

literature, where Rohde & Barrett showed that the balanced strategy [52], where one preferentially bonds cluster states of equal size, is optimal for state growth. In this instance, the only probabilities of interest are $P_{\text{sub}}(s|m,m)$, and the optimized growth probability is $P_{\text{opt}}(m,m) = 1/2 \; \forall \, m$. That is, for every fusion operation between two states of equal size, the probability of growing the state is always $1/2$, which is very favorable when dealing with large photon-number states. When not employing recycling (i.e. accepting only the $s = 0$ outcomes), the growth probability is maximized when we only attempt to fuse a Fock state with the single-photon state (i.e. $m = 1$ or $n = 1$). Rohde & Barrett refer to this as the modesty strategy, since fusions involve only the smallest states.

Clearly, if we were to progressively build up a large photon-number state by repeatedly utilizing the fusion operation and requiring $s = 0$, the success probability of the protocol would decrease exponentially with the number of fusion operations. To improve on this, we borrow the concept of recycling from cluster state protocols [52–54], where when a fusion operation fails we do not throw away the state and begin from scratch, but rather store the states from failures and reuse them in future fusion operations. Intuitively, we are accepting all detection events, as opposed to only the $s = 0$ events, which one expects to improve efficiency.

3.5.1 Fusion Protocol

Assume that an inexhaustible resource of single-photon states is given, i.e. these states are trivial to prepare on-demand. Next, there is a series of state storage buckets (quantum memories) containing Fock states of differing photon numbers. Let $c_n(t)$ be the number of n-photon states that are contained in the respective bucket after the tth fusion operation. Since it is assumed that single-photon states are provided for free, we let $c_1(0) = \infty$, and initialize all other buckets to be empty, $c_{i>1}(0) = 0$.

Then take two Fock states of photon number m and n from the buckets and apply the fusion operation between them. With probability $P_{\text{sub}}(s|m,n)$ this operation prepares the
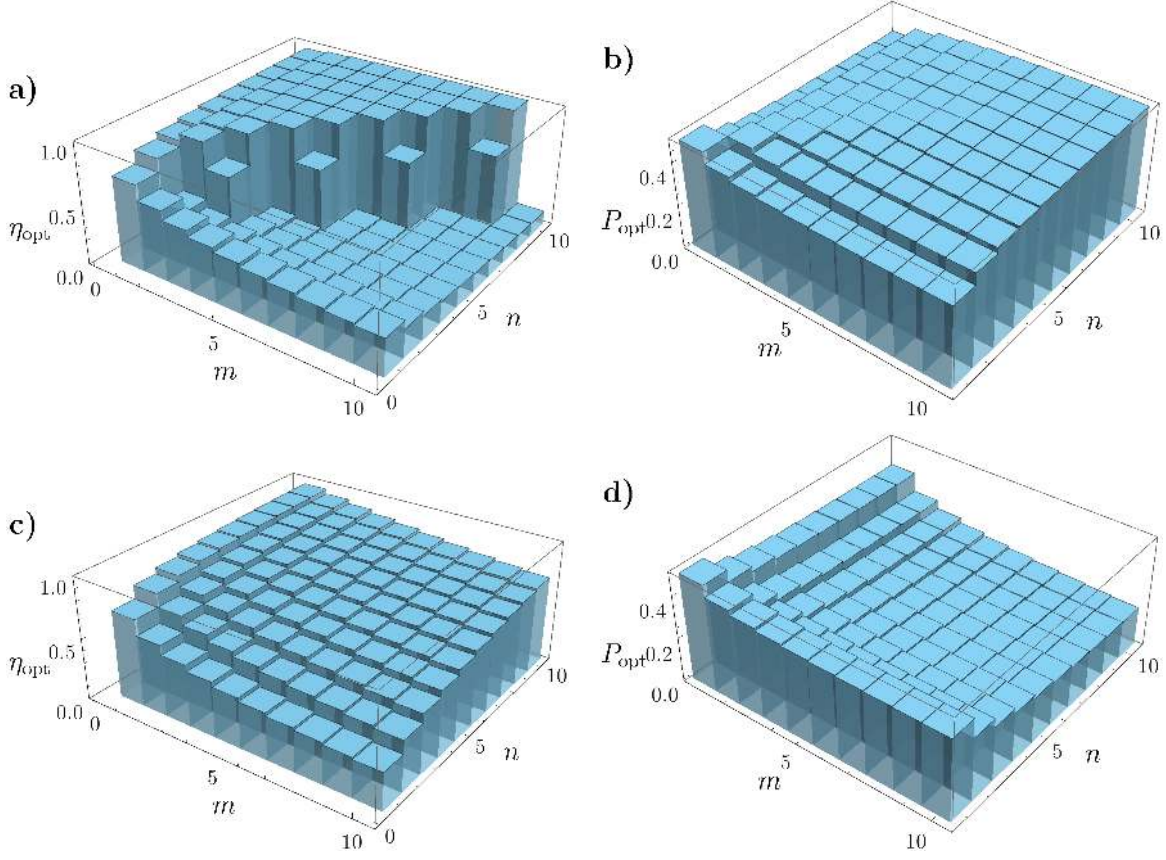
Figure 3.5. (a) The optimal beamsplitter reflectivity (η_{opt}) for maximizing growth probability when fusing two Fock states of photon number m and n, accepting all outcomes s. (b) The associated growth probability (P_{opt}) for the fusion operation. (c) The optimal beamsplitter reflectivity for maximizing only the probability of the $s = 0$ outcome, i.e. for the non-recycled protocol. (d) The associated success probability. Evidently the fusion operation with recycling has higher success probability than without recycling, since we are accepting all events s as opposed to only the $s = 0$ cases.

$(m + n - s)$-photon Fock state, which updates the remaining states in the buckets as

$$
\begin{aligned}
c_m &\rightarrow c_m - 1, \\
c_n &\rightarrow c_n - 1, \\
c_{m+n-s} &\rightarrow
\begin{cases}
c_{m+n-s} + 1 & \text{with recycling;} \\
c_{m+n-s} + \delta_{s,0} & \text{without recycling.}
\end{cases}
\end{aligned}
\tag{3.20}
$$

That is, a state is removed from each of the m- and n-photon buckets, and one more state is added to the $m + n - s$ photon bucket. Thus, the fusion protocol proceeds as a random

walk of state populations among the buckets. With recycling, all events s are accepted, and without recycling only the $s = 0$ outcomes are accepted. Clearly the latter case repopulates the larger buckets with lower probability, which reduces the rate of state preparation.

Now, suppose the goal is to prepare a population of Fock states with photon number of size d or greater. Then the buckets of interest are

$$c_{\geq d} = \sum_{j=d}^{\infty} c_j. \tag{3.21}$$

Then the rate at which these states are prepared, per fusion, is then

$$r(d) = \lim_{t \to \infty} \frac{c_{\geq d}(t)}{t}, \tag{3.22}$$

where the number of fusion operations that have been applied is denoted t. Considering the limit $t \to \infty$ establishes the steady state flow of states through the buckets as the random walk occurs.

3.5.2 Analytic Approximations

For simplified schemes, analytic results are established that show that the rate is exponentially improved over the single-shot case discussed in Sec. 3.3. First a non-recycled scheme is considered, having the goal to construct a Fock state of size d photons, where d is a power of 2. For values of d which are not a power of 2, simply construct a Fock state that is the next largest power of 2. The rate of production will be unchanged, and the scaling is not significantly affected.

Being that this is a non-recycled scheme, only successes are retained. Single-photon states are continually fused until 2-photon states are obtained, then fuse 2-photon states until 4-photon states are obtained, and so on, which the motivation for considering powers of two. As found above (see Fig. 3.5), the probability of success is maximal for 50/50 beam splitters when utilizing equal photon numbers, so 50/50 beam splitters are used. To estimate

the rate, first estimate the average number of single-photon states necessary to produce one d-photon state. Then the rate of preparation for d-photon Fock states per *fusion operation* has scaling equal to the inverse of this number. This holds true because there can be no greater than a factor of 2 between the number of input single-photon states used and the number of fusion procedures.

To demonstrate this, consider first the ideal case wherein every fusion operation is successful. Then for d single-photon inputs, there would be $d/2$ fusion operations, $d/4$ fusion operations on the two-photon states, and so forth. Combining these states together for d being a power of two gives a sum total number of fusion procedures equal to $d-1$, which is one less than the total number of single-photon inputs. As the success rate reduces, the number of fusion operations can only reduce for a given number of single photons. Hence the number of fusion procedures cannot be any larger than the number of input single photons. In this scheme fusion operations are performed on all pairs of single photon Fock states, so the number of fusion operations required must be at least half the number of single-photon states.

Now the average number of single-photon states required to produce one d-photon state is estimated. To fuse two $d/2$-photon states to produce the d-photon state, the expected number of attempts will be $1/P_{\text{sub}}(0|d/2,d/2)$. This corresponds to having an expected number of $d/2$-photon states of $2/P_{\text{sub}}(0|d/2,d/2)$, since there are two in each attempt. Thus, the expected number of $d/4$-photon states required to yield each $d/2$-photon state is $2/P_{\text{sub}}(0|d/4,d/4)$. Further, the expected number of $d/4$-photon states required to create one d-photon state is $4/[P_{\text{sub}}(0|d/2,d/2)P_{\text{sub}}(0|d/4,d/4)]$. Iteratively, the expected number of single photon inputs required to produce one d-photon state is

$$\prod_{j=1}^{\log_2 d} \frac{2}{P_{\text{sub}}(0|d/2^j, d/2^j)}. \tag{3.23}$$

To estimate the expected number of photons from these inputs, we use

$$P_{\text{sub}}(0|n,n) = 2^{-2n}\frac{(2n)!}{(n!)^2} \sim \frac{1}{\sqrt{\pi n}}, \tag{3.24}$$

where the approximation is via Stirling's formula. Combining this approximation with Eq. (3.23) yields the expected number of single-photon states that scales

$$
\begin{aligned}
2^{\log_2 d}\prod_{j=1}^{\log_2 d}\sqrt{\pi d/2^j} &= d(\pi d)^{(\log_2 d)/2}2^{-\log_2 d(\log_2 d+1)/4} \\
&= d^{3/4+(\log_2 \pi)/2+(\log_2 d)/4}. \tag{3.25}
\end{aligned}
$$

Numerically testing this expression, the expected number of single photons is found to be about 1.2777 times this value.

As previously discussed, the rate of preparation for d-photon Fock states per fusion operation scales as the inverse of this expression, and is thus

$$r(d) \propto \frac{1}{d^{3/4+(\log_2 \pi)/2}d^{(\log_2 d)/4}}. \tag{3.26}$$

Theis is an exponential improvement over the single-shot case. The scaling is not exponential in d, however it is also not polynomial in d, given that the exponent is logarithmic in d.

For further improvement, limited recycling can be implemented. Rather than simply requiring no loss at each stage, allow that the number of lost photons is no greater than $n/2$ when fusing two n-photon states such that the probability of success is given by

$$\mathcal{P} = \sum_{s=0}^{\text{Floor}(n/2)} P_{\text{sub}}(s|n,n), \tag{3.27}$$

with $\eta = 1/\sqrt{2}$. Then the probability of success is found numerically and approaches $\sim 1/3$ in the limit $n \to \infty$ as shown in Fig. 3.6. If the photon number is larger than the target, reduction of the photon number can be done with the state reduction scheme described in

Sec. 3.6. Now, in order to obtain the target photon number d, a number of levels that scales as $\log_{3/2} d$, rather than $\log_2 d$, is needed. However, the multiplying factor in the number of repetitions for each stage is smaller.
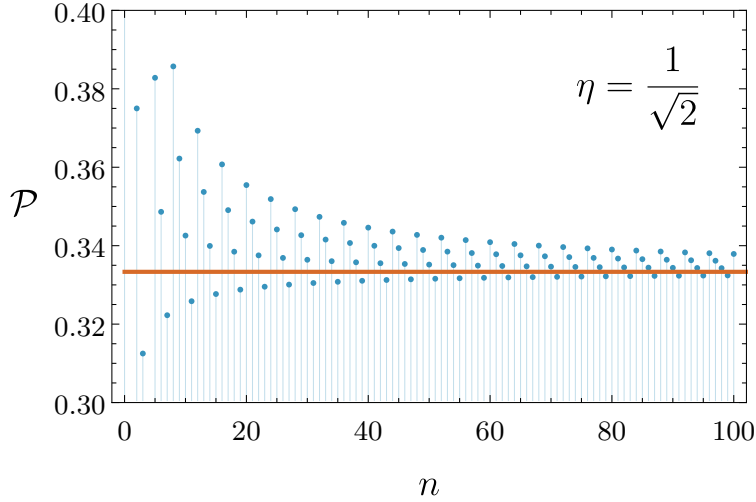

Figure 3.6. The probability of the improved recycling scheme with $\eta = 1/\sqrt{2}$, where the number of photons lost is no more than $n/2$ when fusing two n-photon states. Observe that this probability approaches $\sim 1/3$ as $n \to \infty$.

Therefore, the number of single photons necessary to obtain the target d-photon Fock state scales as

$$6^{\log_{3/2} d} = d^{\log_{3/2} 6} = d^{4.419\cdots}. \tag{3.28}$$

Numerically testing this expression, the number of single photons necessary is about 47 times less. The corresponding rate for this method then scales as

$$r(d) \propto d^{-4.419\cdots}. \tag{3.29}$$

This scaling is another exponential improvement over that of the the single-shot preparation, and is now strictly polynomial.

3.5.3 Fusion Strategies

An analytic bound for the more advanced recycling strategies is highly nontrivial and instead these protocols are simulated as classical Markov processes occuring between the buckets, with transition probabilities given by the parameters $P_{\text{sub}}(s|m,n)$, and transition rules from Eq. (3.20).

While Fig. 3.5 intuitively suggests that the balanced strategy might be optimal, considering several other strategies as a comparison provides further insight into the importance of the fusion strategy. Consider four recycling strategies in total:

- Balanced: Fuse the largest two available states of equal size, $m = n$. This strategy is based on the observation of Fig. 3.5 that fusing states of equal size maximizes the growth probability, P_{grow}.

- Modesty: Always attempt to grow our state by a single photon, by fusing the state m with a single-photon state, $n = 1$.

- Random: Randomly choose any two available states, irrespective of their relative sizes.

- Frugal: Same as balanced, except that it does not attempt to fuse two equally sized states if $m = n > \lfloor d'/2 \rfloor$, where $d' \geq d$. For states of size $n > d'/2$, it instead attempts to fuse available states such that $d \leq m + n \leq d'$. This is because larger number states are costly to prepare, so it is wasteful to fuse two states with a total photon number well in excess of the target d.

The optimization approach for the frugal strategy differs from the other strategies, which utilize P_{grow} as a metric. If the total input photon number $m + n \geq d$, then for each combination of input Fock states m and n, we optimize η to optimize the probability of yielding at least d photons. Specifically, we maximize

$$\sum_{s=0}^{m+n-d} P(s|m,n). \tag{3.30}$$

If $m + n < d$, then for each configuration of input Fock states m and n, we optimize η to maximize the probability of enlarging the maximum photon number. Specifically, we maximize

$$\sum_{s=0}^{m+n-\max(m,n)} [m + n - s - \max(m,n)]P(s|m,n).$$

(3.31)

3.6   State Reduction

With d as the target number of photons, the state preparation rate $r(d)$ is then defined to be the rate at which states of photon-numer *at least* d are prepared. For some protocols requiring large Fock states, this is an appropriate definition. However, in other applications one may desire states of size *exactly* equal to d. This case requires a protocol by which to reduce the photon number of output states larger than d to then photon number states of size exactly d.

This is most easily implemented using post-selected linear optics. Simply input the prepared over-sized Fock state on a very low-reflectivity beamsplitter and inject vacuum at the other input ($n = 0$, $\eta \ll 1$). Since the beamsplitter reflectivity is low, the reflected mode will contain no photons most of the time. Sometimes, however, a single photon will be detected. With higher order probability, occasionally more than one photon will be detected. By reducing the reflectivity to sufficiently small value, these higher-order probabilities may be made arbitrarily low, yielding close to unit probability we detect at most one photon. It is in this case that the photon number has been reduced by one. Repeated application of this protocol until the desired number of photons have been subtracted will result in the Fock state of the target size. This protocol is efficient, requiring $O(s)$ beamsplitter procedurs on average when attempting to remove s photons.
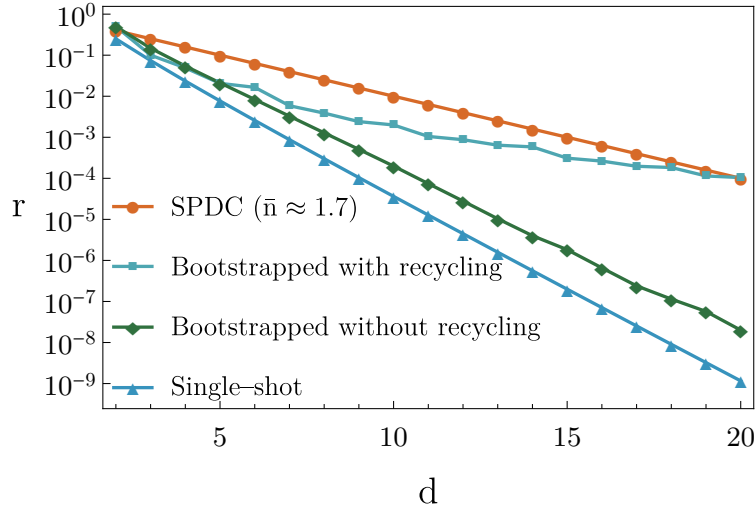
3.7 Results

Figure 3.7. Preparation rate r of Fock states of size at least d photons, for various strategies

In Fig. 3.7, the rate of d-photon state preparation, $r(d)$, is plotted for both the recycled and non-recycled bootstrapped protocols (Sec. 3.4), the single-shot protocol (Sec. 3.3), and heralded SPDC (Sec. 3.2).

In both of the bootstrapped protocols the balanced fusion strategy is employed and an infinite resource of single-photon states is assumed, $c_1 = \infty$. Here the resource of interest is the number of fusion (i.e. beamsplitter) operations.

In the case of the single-shot protocol, Eq. (3.11) gives the rate of state preparation in terms of the number of trials of the entire interferometer. To convert this to the resource of number of beamsplitters, recognize that the interferometer shown in Fig. 3.3 can be most easily constructed out of d beamsplitters in a linear array to progressively route each photon to the top mode. Thus, the state preparation rate, as measured by number of beamsplitters, is simply given by Eq. (3.11) with an additional factor of $1/d$, resulting in $r(d) = d!/d^{d+1}$.

In heralded SPDC, there is no direct conversion of resource requirements, since SPDC protocols employ neither beamsplitters nor single-photon states as a resource. Rather, the resource is the number of repeated trials of the SPDC source (equivalent to the pump repetition rate). Thus, the number of repetitions is used as the resource, with the caveat that this

resource has a slightly different interpretation than the resource usage in other protocols. In Fig. 3.7, the mean photon-number, $\bar{n}$, has been chosen such that SPDC has the same 20-photon preparation rate as the balanced bootstrapped protocol with recycling, in which case it's clear that $\bar{n} \approx 1.7$ is a threshold, above which SPDC has a more efficient preparation rate than the recycled bootstrapped protocol, but below which SPDC is less efficient. This threshold for mean photon number is well beyond what is typically employed in present-day experiments.

It is clear from the log plot that in all schemes other than the balanced recycled protocol, the state preparation rate decreases exponentially in d. However, it is evident that employment of recycling substantially improves the preparation rate compared to non-recycled and single-shot approaches. As an example, in 20-photon state preparation, state recycling improves the rate of preparation by a factor of $\approx 10^5$ over the single-shot protocol.
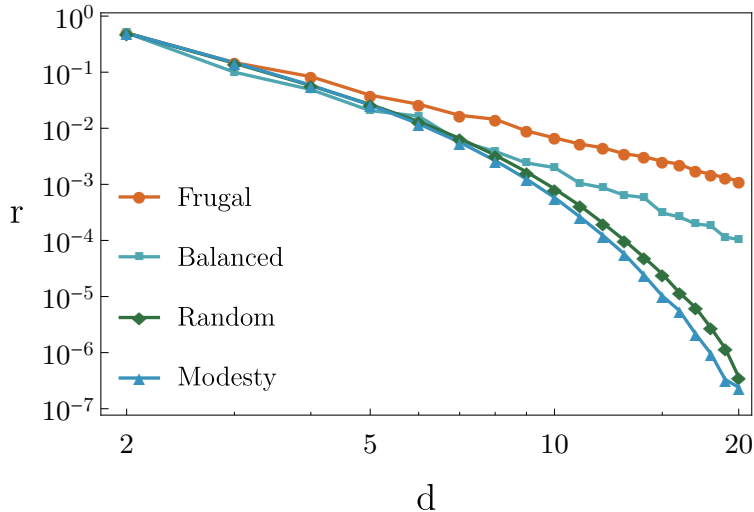

Figure 3.8. Comparison of each strategy when employing recycling of fused states, showing the strategies frugal, balanced, random, and modesty.

In Fig. 3.8, the recycled protocol of the various fusion strategies discussed earlier in Sec. 3.5 is shown. From the log log plot, it is apparent that the preparation rate displays polynomial scaling with d when employing frugal or balanced recycled strategies, opposing the exponential scaling of the random and modesty recycled strategies as well as the single-

shot, non-recycled and SPDC . This represents an exponential improvement in efficiency for the frugal and balanced recycled protocols. The associated scaling in the Frugal and Balanced strategies scales as $\sim 1/d^{2.8}$ and $\sim 1/d^{3.7}$ respectively, which is significantly better than the scaling of the doubling approach that yielded the rate in Eq. (3.29).

3.8 Conclusion

A scheme for preparing large Fock states non-deterministically from a resource of single-photons has been presented. This schemes uses post-selected linear optics, by progressively fusing smaller Fock states into larger ones. By employing state recycling the state preparation rate is shown to be exponentially improved — orders of magnitude for large Fock states — allowing experiments to, in polynomial time, prepare much larger photon-number states than naïve brute-force, single-shot methods, which require exponential time in general. Some of the experimental requirements, such as quantum memory and fast feed-forward, are presently challenging, however these requirements are nearly the same as those for LOQC. Thus, as the tools for optical quantum computing become experimentally realistic, all requirements for this scheme will be in place, and so new experiments requiring large Fock states will be accessible.

In the analysis, the ideal case is considered, where the resource of single-photon states are perfect single-photon states (or, more generally, $|x\rangle$ when x-photon states are used as a resource), and the photo-detectors, beamsplitters and quantum memory have perfect efficiency. In reality, any experimental implementation will suffer from inefficiencies, which will result in the output states being mixed in the photon-number basis, something which future experimental implementations will need to take into account.

Regarding the detector efficiency issue, in the next chapter I discuss how one can exploit the statistics of the TMSV state to calibrate a single-photon (bucket) detector without need for a calibrated reference detector.

4 Calibration of Single-Photon Detectors

4.1 Motivation and Background

Photon-number information is required for many applications of quantum optics such as linear-optical quantum computing [59, 60], super-resolution [61], super-sensitive microscopy [62], foundations of quantum mechanics [63], and quantum key distribution [64]. There are a few techniques to date to measure photon-number [65]. A leading approach is to utilize single photon detectors (SPDs) with a network of beam-splitters to separate photons into separate SPDs (spatial multiplexing) or as an array of SPDs [66]. It is also known that a single SPD can be used if the beam-splitters separate the photons into distinct time slots (time multiplexing) [67]. The combined signal from all SPDs is then summed, yielding the photon-number information. Though multiplexing techniques provide this information, they are not considered as true photon-number-resolving (PNR) detectors due to saturation of the system at the elements [68]. We use "multiplexing PNR detectors" as a generic label for time multiplexers, spatial multiplexers and SPD arrays throughout this chapter.

To gain precise photon-number information about the measured quantum state, the detector must be characterized; in particular, its detection efficiency must be measured. Characterization of the detector's efficiency is here considered to be calibration of the device. The industry-standard procedure to calibrate SPDs is to utilize correlated photon pairs from a TMSV state. This method was first suggested in 1977 by Klyshko [69] and shown experimentally two years later by Kitaeva [70]. For this method, two detectors are required because the coincidence rate must be known in order to calculate the efficiencies. Recently, this method was adapted to PNR detectors [71–73].

Other methods exist to calibrate the detection efficiency [74, 76]. One such method uses only a single SPD, which is time-multiplexed to separate the incident photons temporally [74]. The detection efficiency is then found as in the two detector method. In this chapter, a model

This bulk of the work in this chapter appeared previously as Ref. [75] published under Copyright © 2018 by the American Physical Society

is developed to characterize a multiplexing PNR detector. The analysis is then applied to calibration of a single SPD. With the unique photon-number statistics of the single-mode and two-mode squeezed vacuum states (SMSV and TMSV, respectively), the detection efficiency is shown to be found without a reference detector or any form of multiplexing.

This chapter is arranged as follows: first, a model for the general multiplexing PNR detector is presented in Sec. 4.2. In Sec. 4.3 the discussion is limited to one SPD and it is shown how the efficiency can be measured using SMSV and TMSV light. The setup to perform the calibration is also described there. The calibration procedure results are presented in Sec. 4.4. There, a comparison between the use of SMSV and TMSV is demonstrated.

4.2 Model of Characterization

Given a multiplexed PNR detector, there is a problem presented by attempting to count the photon number of an input state due to several internal noise effects distorting the measurement statistics [77]. The incident photon statistics can be reconstructed, however, if proper care is taken to quantify the distortion effects. Several detection parameters are considered: efficiency, total number of SPD elements (finite detector size), dark-count rate, and cross-talk rate. Particularly, the combined effects of finite-size with cross-talk were not well known prior to this work [78]. Now, an analytical model is presented which incorporates all of these effects.

4.2.1 Detector Loss

When a photon strikes a multiplexed PNR detector, there is a probability greater than zero that either the diode avalanche process will fail to start or will stop before a detection occurs [79]. This is an intrinsic flaw of any realistic sensor, but can equivalently be attributed to inefficiency in coupling light to the device. In this scenario, the photon is considered to be lost. The detection efficiency is thus defined as the probability for detecting a single photon, given that a single photon was incident upon the PNR detector. The detection efficiency is assumed to be uniform for all SPD elements in the multiplexed device and is denoted by η.

If n photons strike the detector, the probability of m elements being activated is given by a binomial distribution [77]:

$$M_{loss}^{\eta}(m, n) = \binom{n}{m} \eta^m (1 - \eta)^{n-m} \, , \tag{4.1}$$

where $\binom{n}{m} = \frac{n!}{m!(n-m)!}$ for $n \geq m \geq 0$ or zero otherwise. Here it is assumed that each photon strikes a different element. This assumption is in general not valid but will be corrected for later by including the effects of finite detector size.

4.2.2 Finite-size Effects

An SPD constitues an individual element of the multiplexed PNR. As such, the signal from each element shall not depend on the number of photons hitting it. Therefore, if more than one photon strikes an individual element, only one can be detected, inducing a non-linear loss of photons and a distortion of the incident photon statistics. The probability that m photons strike k different elements of an N-element detector, is given as [80]:

$$M_{FS}^{N}(k, m) = \frac{1}{N^m} \binom{N}{k} k! S(m, k) \, , \tag{4.2}$$

where $S(m, k) = \frac{1}{k!} \sum_{j=0}^{k} (-1)^{k-j} \binom{k}{j} j^m$ are the Stirling numbers of the second kind [81].

4.2.3 Dark-count Errors

When k elements fire due to photon detection events, there are a remaining $(N - k)$ elements which are free to fire due to a dark-count – a false event in which the detector fires despite the lack of an incident photon. This typically occurs due to thermal electrons in the material. It is assumed that each element has equal (and constant) probability d for this event to occur.Then p is defined to be the total number of elements that fire in sum,

including those elements which report a dark count. Thus the number of elements that fire due a dark-count error is $p - k$. Finally, the probability for this many elements to be activated due to dark-counts where $(N - k)$ elements are available is given by

$$M_{DC}^d(p, k) = \binom{N - k}{p - k} d^{(p-k)}(1 - d)^{N-p}. \tag{4.3}$$

4.2.4 Cross-talk Events

The last error to consider is perhaps the most complicated – cross-talk. Cross-talk is an effect in which a recombination of an thermally-excited electron and its corresponding hole generates a photon which is detected by a non-activated neighboring SPD [82]. All multiplexing PNR detectors suffer from this effect but, the effects are negligible when the SPDs are distant and the cross-talk counts can be temporally filtered. Therefore, cross-talk is most likely to happen at only nearest-neighbor elements and other scenarios are neglected.

A few cross-talk models are available in the literature [77, 83–85], however each has its own advantages and disadvantages and none of them additionally incorporates the effects of the finite size of the detector. Thus, a new model for the cross-talk is introduced.

Until this point, the only assumption has been uniformity of the constituent SPDs in the multiplexed PNR detector. However, in order to analytically solve the cross-talk effects, more assumptions must be made. The cross-talk probability strongly dependents on the number of non-activated neighbors, but it is impossible to know *a priori* how many nearest neighbors are available to fire. Instead, the effective number of nearest neighbors that are available on average ENN is computed. When p elements are already activated, this number is given by $\text{ENN} = 4(1 - \frac{p}{N})\frac{N - \sqrt{N}}{N-1}$. As a sanity check, this linearly dependent formula is reasonable as it is zero if no elements are available and thus $(p = N)$. In the other limit, if all elements are available to fire then ENN nears four, a limit imposed by the rectangular shape of the detector's edge. This formula is derived by simply choosing p random elements

and counting their nearest neighbors, then average over many different configurations.

The probability for cross-talk to one of the available nearest neighbors is denoted x. Terms proportional to higher powers of x are neglected by assuming $x \ll 1$. In particular, cross-talk generated by another cross-talk event as well as events with more than one cross-talk event generated per element as neglected. Thus, the probability for a single element to generate a cross-talk event is $4x(1 - \frac{p}{N})\frac{N-\sqrt{N}}{N-1}$ and for p distinct elements to generate ℓ cross-talk events is simply a binomial combination. Under these assumptions, the probability of $(s - p)$ elements being activated by cross-talks from p elements is,

$$M_{XT}^{\tilde{x}}(s,p) = \binom{p}{s-p} \left(\tilde{x} \left(1 - \tfrac{p}{N}\right) \right)^{s-p} \left(1 - \tilde{x} \left(1 - \tfrac{p}{N}\right) \right)^{2p-s}$$

(4.4)

where $\tilde{x} = 4x\frac{N-\sqrt{N}}{N-1}$.

4.2.5 Detection Statistics

The real photon number probabilities $(\vec{P}_{\text{real}})$ is simply related to the photon number probabilities $(\vec{P}_{\text{det}})$ the are detected by

$$\vec{P}_{\text{det}} = \mathbf{M}_{XT} \cdot \mathbf{M}_D \cdot \mathbf{M}_{FS} \cdot \mathbf{M}_L \cdot \vec{P}_{\text{real}},$$

(4.5)

where $\mathbf{M}_{XT}, \mathbf{M}_D, \mathbf{M}_{FS}, \mathbf{M}_L$ are matrices quantifying cross-talk, dark-counts, finite-size (edge) and loss effects, respectively.

The detected statistics for an n-photon Fock state, a state with a fixed number of n photons, are calculated first; Then, any other state can generalized to by averaging the results over the actual photon statistics. The probability for s detection events to occur due to incident n-photon Fock states after accounting for all distortion effects is,

$$P_{\text{det}}^n(s|\eta, d, N, \tilde{x}) = \tag{4.6}$$

$$\sum_{p=0}^{s} \binom{p}{s-p} \left(\tilde{x}\left(1-\frac{p}{N}\right)\right)^{(s-p)} \left(1-\tilde{x}\left(1-\frac{p}{N}\right)\right)^{2p-s}$$

$$\binom{N}{p} \sum_{j=0}^{p} \binom{p}{j} (-1)^{p-j}(1-d)^{N-j} \left(1-\eta+\frac{j\eta}{N}\right)^{n}.$$

This result is proven in appendix B.1 and agrees with previous analytical results when substituting $\tilde{x} = 0, d = 0$ [80] and $\eta = 1$ [67].

4.3 Experimental Setup

From this point only a single SPD is considered, i.e. $N = 1$. In this case, there are only two detection possibilities; there is either the SPD fires or not. Mathematically it means $s = 0$ or $s = 0$ in Eq. 4.6, and therefore the cross-talk summation vanishes.

In order to calibrate the detector, both the single-mode squeezed vacuum (SMSV) and two-mode squeezed vacuum (TMSV) states have been used, with a calibrated and adjustable attenuator on the SV light. Although only one of these states is required, either scheme will work for calibration purposes. The attenuated SV light is directed to a bandpass filter, then sent into a single-mode fiber that is coupled into the SPD. If a TMSV state is used, the separate modes are set to orthogonal polarizations and then spatially combined using a polarizing beam splitter (PBS) (see Fig. 4.1).

It is here convenient to define the odds $O_{\text{det}}^n(\eta, d, 1, 0) \equiv \frac{P_{\text{det}}^n(s=1|\eta,d,1,0)}{P_{\text{det}}^n(s=0|\eta,d,1,0)}$ of a detection event. Then rewrite $\eta \to \eta t$, where t is the transmission of the properly-calibrated adjustable attenuator, and now henceforth η is defined to be the fixed efficiency and t is a variable. With these changes, Eq. 4.6 is now reduced to:

$$O_{\text{det}}^{\text{SMSV}}(\eta t, d, 1, 0) = \left(\frac{\sqrt{1 + (2-\eta t)\eta\bar{n}t}}{1-d} - 1\right) \approx \frac{(1-\frac{\eta t}{2})\eta\bar{n}t + d}{1-d}, \tag{4.7}$$

$$O_{\text{det}}^{\text{TMSV}}(\eta t, d, 1, 0) = \frac{(1 - \frac{\eta t}{2})\eta \bar{n} t + d}{1 - d} \ . \tag{4.8}$$

Here Eqs. 4.7 and 4.8 correspond to SMSV and TMSV states, respectively. The approximation is merely the Taylor expansion for $\bar{n} \ll 1$; the full derivation is given in appendix B.2.

Experimentally, the detection probability is given by the ratio of the number of detections to the number of incident pump pulses. This probability is measured while varying the transmissivity of the Neutral Density Filter (NDF). The detection efficiency parameter is then obtained from a second-order fit to Eq. 4.7 or Eq. 4.8.

The experimental setup is described in Fig. 4.1. Identical $780\,\text{nm}$ photon pairs are generated by a SPDC process from a $2\,\text{mm}$ thick β-BaB_2O_4 (BBO) crystal using a $390\,\text{nm}$ Ti:Sapphire pulsed laser. In the first part, we have used collinear type-I SPDC to generate a horizontally-polarized SMSV state. In the second part, we have used non-collinear type-II SPDC to generate the TMSV state. The two modes of the TMSV state have been set in orthogonal polarizations, and spatially combined via a PBS. For comparison, an additional SPD has been used to confirm detection efficiency by using the standard two-detector method. For clarity, a dashed line indicates the beam path to the reference detector, where a beamsplitter (BS) or half-wave plate (HWP) were added to divert photons to the reference detector. Note that a calibrated NDF is used as a convenient method for a known attenuation. Any other self-calibrated attenuation method could be used instead; for instance, the attenuation of SMSV can be realized by a single rotating polarizer.

4.4 Results

The present scheme is useful for evaluating the detector efficiency of a SPD, due to the unique photon-statistics of the SV light as well as the non-linear loss of the SPD. The non-linear loss distorts the linear dependency of the single-photon counts on the attenuation and then detection efficiency is extracted from the curvature.

SPD counts were accumulated for one second over a range of 40 different values of at-

tenuation due to the NDF. The probability for a photon detection is then computed by the single counts divided by the total number of incident pulses. We repeat the experiment for two individual SPDs using both SMSV and TMSV in order to demonstrate that detectors of different efficiency can be calibrated in this way. The results are presented in Fig. 4.2. The data is fit to a second-order polynomial $a_2 t^2 + a_1 t + a_0$ in each of the four measurements. According to Eqs. 4.7 and 4.8 the efficiency is then $\eta = -2\frac{a_2}{a_1}$.

In table 4.1 the results for the single detector method are summarized. Those results are compared to the standard two-detector method, showing good agreement between the two distinct methods for all detectors used and for both distinct experimental setups. The detection efficiency is incidentally lower in the SMSV setup due to weaker fiber coupling to the detector, which is likely a result of the spatial walk-off inside the non-linear crystal. The inefficient coupling is a loss-factor observed in both calibration methods.

In order to show the presented method is valid for all pump intensities, the experiment is repeated using TMSV and SPD #1 for varying pump intensities. The results of this process are plotted in Fig. 4.3. As done previously, the efficiency is calculated from the polynomial coefficients from a second-order polynomial fit.

The results for different pump intensities are summarized in table 4.2. A good agreement is observed between varying pump powers, where a standard deviation of 0.5% is observed.

4.5 Conclusion

A model to characterize a PNR detector based on SPDs has been presented. This model predicts the detected photon-statistics in the presence of loss, finite size, dark counts and

Table 4.1. The efficiencies measured in both the presented single detector method (η_1) and the two detector method (η_2). Note that in the SMSV case the efficiencies are lower than observed in the TMSV case due to weaker coupling into the single-mode fiber.

SPD #	SV light	η_1	η_2
1	SMSV	$11.3 \pm 1.1\%$	$11.8 \pm 0.9\%$
2	SMSV	$7.4 \pm 0.9\%$	$8.1 \pm 0.9\%$
1	TMSV	$17.4 \pm 1.0\%$	$17.3 \pm 0.8\%$
2	TMSV	$12.7 \pm 0.9\%$	$11.7 \pm 0.8\%$

Table 4.2. The detection efficiencies as measured by the single-detector method (η_1) with SPD1 and TMSV light for varying pump powers.

Pump power	η_1
145 mW	$17.9 \pm 0.8\%$
180 mW	$16.5 \pm 0.9\%$
215 mW	$17.2 \pm 0.8\%$
240 mW	$16.8 \pm 0.7\%$
250 mW	$17.6 \pm 0.7\%$

cross-talk. This model is also shown to be valid for a single SPD, as the predicted detection statistics show an efficiency dependence when detecting SV light. Thus, the efficiency can be extracted without requiring a reference detector. The efficiency of a SPD has been experimentally measured and successfully compared to the two-detector method, demonstrating that the unique quantum statistics of SMSV and TMSV can be exploited to perform a task classically thought impossible.
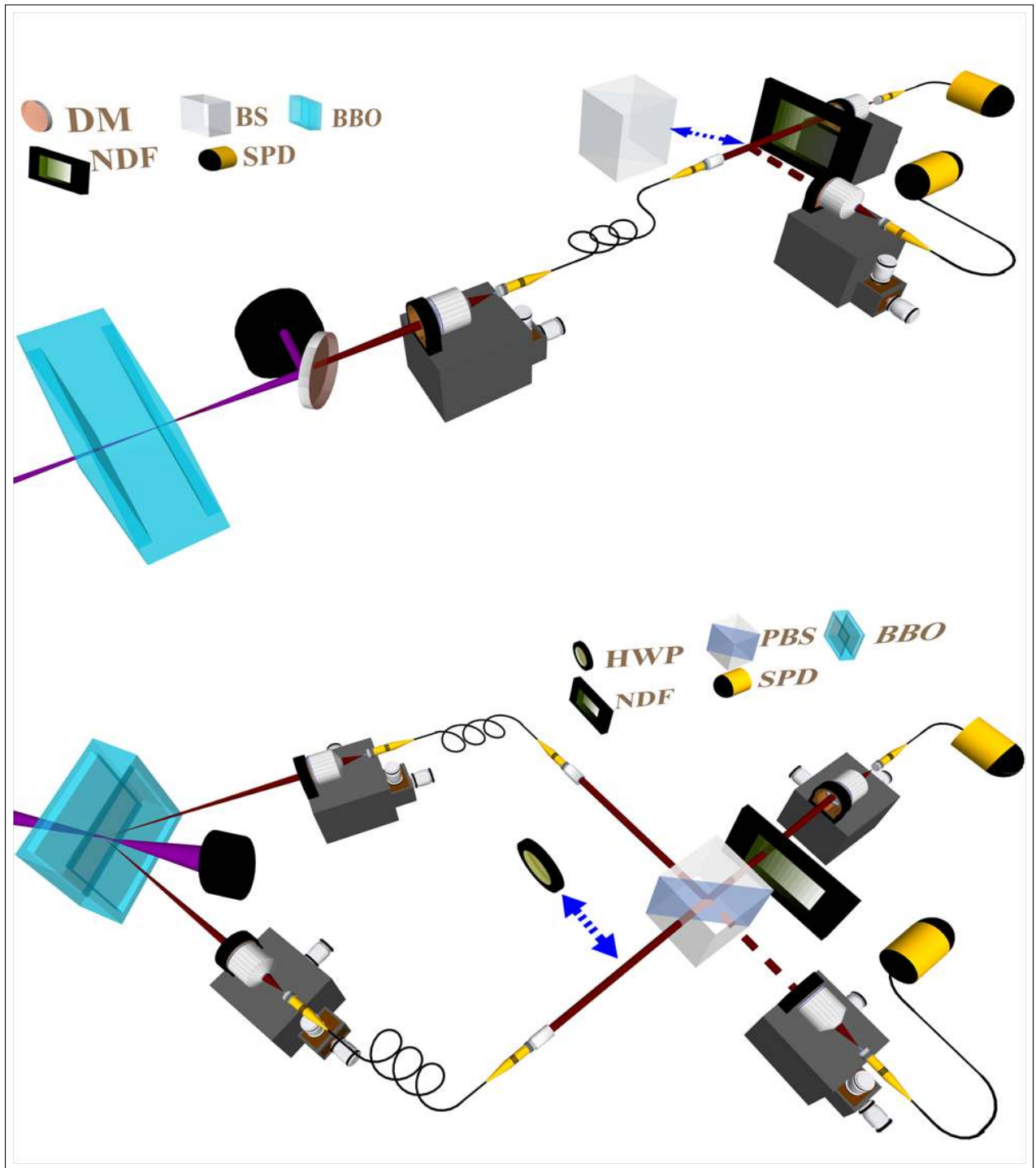
Figure 4.1. The experimental setup. The upper scheme is the setup where the SMSV state is used and the lower scheme is when a TMSV state is used instead. DM - dichroic mirror, PBS - polarizing beam splitter, HWP - half wave-plate, NDF - variable neutral density filter, BD - beam dump. Note that SPD2 serves as a reference of calibration, and is unnecessary for the procedure.
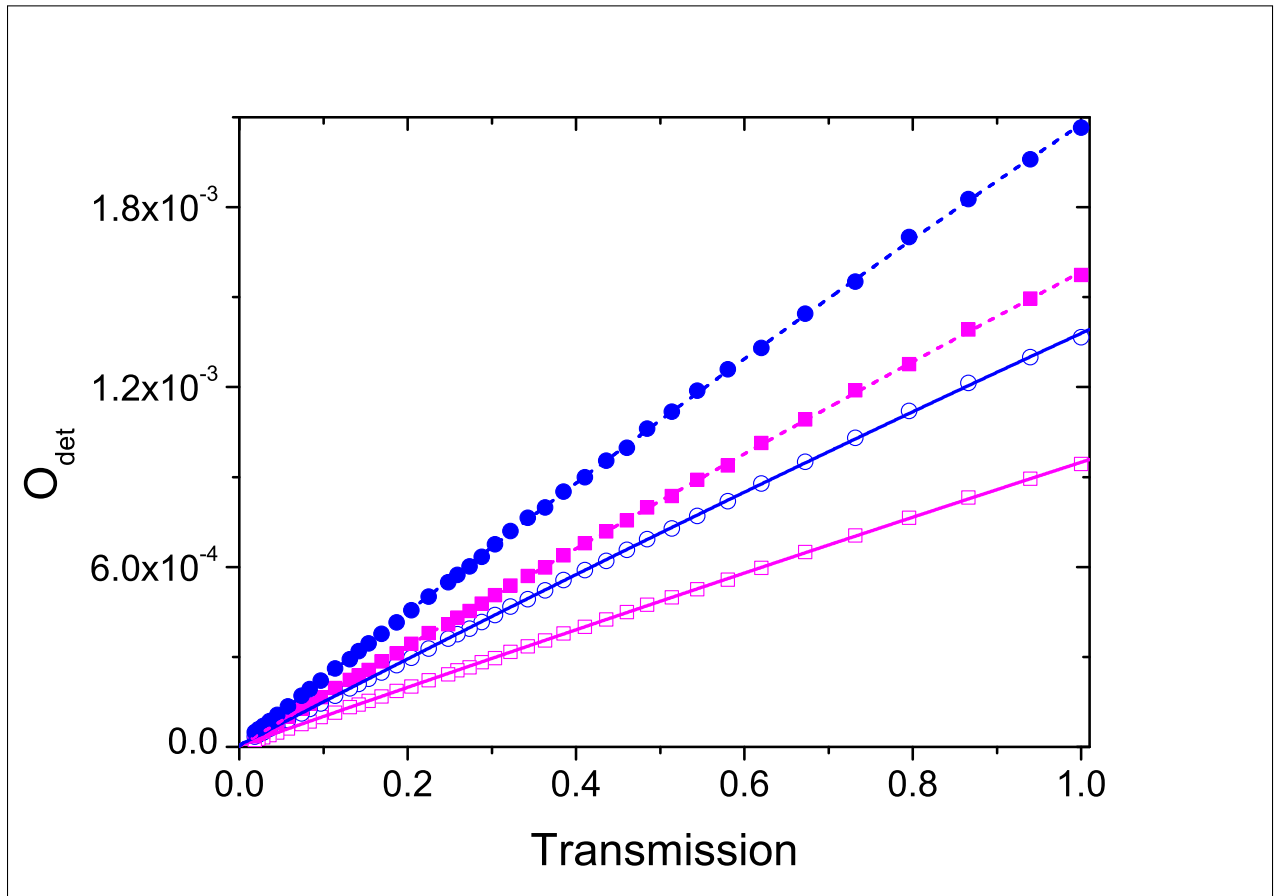
Figure 4.2. The detection event odds as a function of the NDF transmission for two distinct and separate detectors. Solid and empty markers denote data from using TMSV and SMSV, respectively. Solid and dashed curves are fits to Eqs. 4.7 and 4.8, respectively. SPD#1 is represented by blue circles and SPD#2 is represented by pink boxes. Error bars are simply assumed Poissonian noise and are smaller than the symbol sizes, and thus are not displayed.
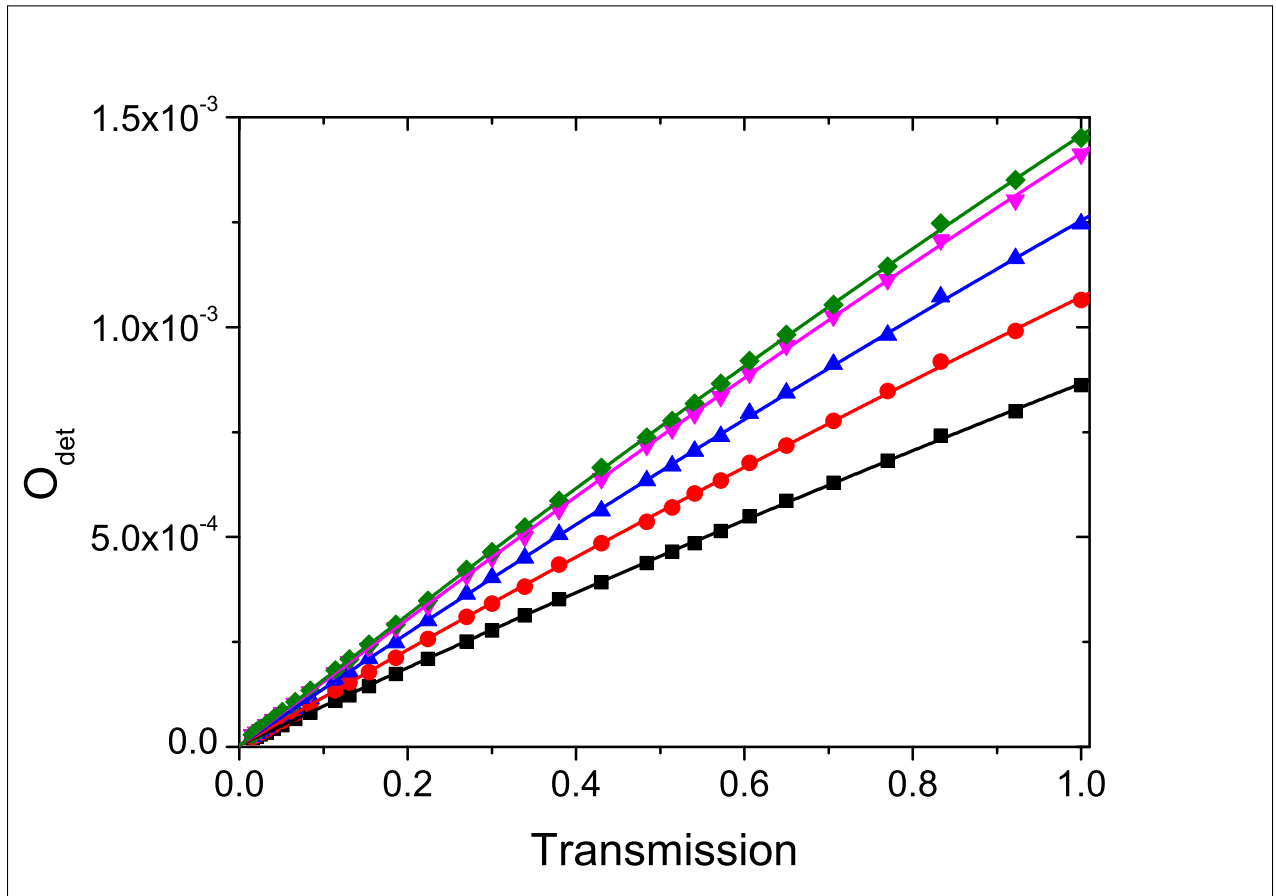
Figure 4.3. The odds of a detection event as a function of the NDF transmission for SPD #1 when the pump power is varied. Green diamonds correspond to pump power of 250 mW, pink downward triangles to 240 mW, blue triangles to 215 mW, red circles to 180 mW and black boxes to 145 mW. Error bars are again assumed to be simple Poissonian noise and are smaller than the symbol sizes, and thus are not displayed.

5 Conclusion

In this thesis, Ch: 1 introduced the concepts of quantum optics, and further explained how these concepts can be exploited to perform sensitive quantum measurements. I have shown how quantum mechanics limits the information we can obtain from a system due to unavoidable fluctuations inherent in all physical states. However, I have also shown how these limits give us metrics to ensure that we extract as much information as nature allows – thereby we are able to discover schemes that we can be sure perform optimal measurements.

Then in Ch: 2 I have covered the problem of quantum optical phase estimation from first principles through a fully-realized system that exhibits sub-shot-noise limited phase sensitivity. I have utilized quantum statistics of light, combined with detection limits given by the quantum nature of light, to compare the QuFTI architecture to other phase-estimation schemes. In doing so, I have shown how one can simply and accurately determine how optimal a given passive linear-optical metrology setup is when compared to limits such as the SNL and the HL.

I have then in Ch: 3 also demonstrated how to prepare an important quantum metrology resource, the Fock states, using a readily-available source of single-photons. The techniques presented have been optimized for production rates and hence will allow for more easily-prepared exotic states, such as N00N states. Though the technological requirements for these schemes are essentially the same as that of the fully-optical quantum computing, once the technology is available these techniques will be ready for application.

Lastly, in Ch: 4 I have demonstrated a clever use of the quantum statistics of light of both single-mode squeezed vacuum and two-mode squeezed vacuum states that allows for calibration of single-photon, as well as photon-number-resolving multiplexed detectors, without the need for a second reference detector. This will enable simpler experimental implementation of quantum metrology schemes.

In summary, I have optimized the generic multi-mode passive linear-optical phase-estimation architecture. I have also developed efficient methods to produce metrologically-useful states

by intelligently using single-photons. A unique way of calibrating a highly-important class of quantum detectors–the single-photon detector–has been demonstrated.

References

[1] C. Gerry and P. L. Knight, *Introductory Quantum Optics* (Cambridge University Press, 2005).

[2] W. B. Case, "Wigner functions and Weyl transforms for pedestrians," *Am. J. of Phys.* **76**, 937 (2008).

[3] Gard, B. T., "Advances in Quantum Metrology: Continuous Variables in Phase Space" (2016) *LSU Doctoral Dissertations* 2089.

[4] C. K. Hong, Z. Y. Ou, and L. Mandel, "Measurement of subpicosecond time intervals between two photons by interference", Phys. Rev. Lett. **59**, 2044 (1987).

[5] R. Demkowicz-Dobrzański, M. Jarzyna, and J. Kołodyński, *Chapter Four – Quantum Limits in Optical Interferometry* (Elsevier, 2015), pp. 345–435.

[6] C. W. Helstrom, *Quantum detection and estimation theory* (Academic press, 1976).

[7] J. P. Olson, K. R. Motes, P. M. Birchall, *et al.*, "Linear optical quantum metrology with single photons: Experimental errors, resource counting, and quantum Cramér-Rao bounds", Phys. Rev. A **96**, 013180 (2017).

[8] K. R. Motes, J. P. Olson, E. J. Rabeaux, *et al.*, "Linear Optical Quantum Metrology with Single Photons: Exploiting Spontaneously Generated Entanglement to Beat the Shot-Noise Limit", Phys. Rev. Lett. **118**, 079901 (2015).

[9] C. You, S. Adhikari, Y. Chi, *et al.*, "Multiparameter estimation with single photons – linearly-optically generated quantum entanglement beats the shotnoise limit", *J. of Optics* **19** 124002 (2017).

[10] J. P. Dowling, "Quantum optical metrology – the lowdown on high-N00N states", Contemp. Phys. **49**, 125 (2008).

[11] P. Kok, W. J. Munro, K. Nemoto, *et al.*, "Linear optical quantum computing with photonic qubits", Rev. Mod. Phys. **79**, 135 (2005).

[12] H. Cable and J. P. Dowling, "Efficient Generation of Large Number-Path Entanglement Using Only Linear Optics and Feed-Forward", Phys. Rev. Lett. **99**, 163604 (2007).

[13] S. Aaronson and A. Arkhipov, "The Computational Complexity of Linear Optics", Proc. ACM STOC (New York) p. 333 (2011).

[14] B. T. Gard, K. R. Motes, J. P. Olson, *et al.* Chapter 8, pp. 167–192, in *From Atomic to Mesoscale: The Role of Quantum Coherence in Systems of Various Complexities.* World Scientific Publishing Co. (2015), Eds. S. A. Malinovskaya, I. Novikova.

[15] S. Scheel, "Permanents in linear optical networks", quant-ph/0508189 or Acta Physica Slovaca **58**, 675 (2008) (2004).

[16] L. G. Valiant, "The complexity of computing the permanent", Theoretical Computer Science **8**, 189 (1979).

[17] M. A. Broome, A. Fedrizzi, S. Rahimi-Keshari, *et al.*, "Photonic Boson Sampling in a Tunable Circuit", Science **339**, 6121 (2013).

[18] A. Crespi, R. Osellame, R. Ramponi, *et al.*, "Integrated multimode interferometers with arbitrary designs for photonic boson sampling", Nat. Phot. **7**, 545 (2013).

[19] M. Tillmann, B. Daki, R. Heilmann, *et al.*, "Experimental boson sampling", Nat. Phot. **7**, 540 (2013).

[20] J. B. Spring, B. J. Metcalf, P. C. Humphreys, *et al.* et al., "Boson Sampling on a Photonic Chip", Science **339**, 6121 (2013).

[21] Y. He, Z.-E. Su, H.-L. Huang, *et al.*, "Scalable boson sampling with a single-photon device", arXiv:1603.04127 (2016).

[22] B. Opanchuk, L. Rosales-Zárate, M. D. Reid, *et al.*, "Quantum software for linear photonic simulations", Phys. Rev. A **97**, 042304 (2018);

[23] J. Carolan, C. Harrold, C. Sparrow, *et al.*, "Universal linear optics", Science **349**, 711 (2015).

[24] S. L. Braunstein and C. M. Caves, "Statistical distance and the geometry of quantum states", Phys. Rev. Lett. **72**, 3439 (1994).

[25] B. L. Higgins, D. W. Berry, S. D. Bartlett, *et al.* and G. J. Pryde, "Entanglement-free Heisenberg-limited phase estimation", Nature **450**, 393 (2007).

[26] R. Demkowicz-Dobrzanski, J. Kolodynski, M. Guta, "The elusive Heisenberg limit in quantum-enhanced metrology", Nat. Comm. **3**, 1063 (2012).

[27] D. W. Berry, B. L. Higgins, S. D. Bartlett, *et al.*, "How to perform the most accurate possible phase measurements", Phys. Rev. A **80**, 052114 (2009).

[28] M. Holland and K. Burnett, "Interferometric detection of optical phase shifts at the Heisenberg limit", Phys. Rev. Lett. **71**, 1355 (1993).

[29] K. R. Motes, R. L. Mann, J. P. Olson, *et al.* arXiv:1603.00533 (2016).

[30] R. Demkowicz-Dobrzański, U. Dorner, B. Smith, *et al.*, "Quantum phase estimation with lossy interferometers", Phys. Rev. A **80**, 013825 (2009).

[31] J. P. Dowling, private communication (2016).

[32] K. R. Motes, J. P. Dowling, A. Gilchrist, *et al.*, "Implementing BosonSampling with time-bin encoding: Analysis of loss, mode mismatch, and time jitter", Phys. Rev. A **92**, 052319 (2015b).

[33] K. R. Motes, A. Gilchrist, J. P. Dowling, *et al.*, "Scalable Boson Sampling with Time-Bin Encoding Using a Loop-Based Architecture", Phys. Rev. Lett. **113**, 120501 (2014).

[34] B. R. Bardan, K. Jiang, and J. P. Dowling, "Effects of phase fluctuations on phase sensitivity and visibility of path-entangled photon Fock states", Phys. Rev. A **88**, 023857 (2013).

[35] P. M. Anisimov, G. M. Raterman, A. Chiruvelli,*et al.*, "Quantum Metrology with Two-Mode Squeezed Vacuum: Parity Detection Beats the Heisenberg Limit", Phys. Rev. Lett. **104**, 103602 (2010).

[36] W. Vogel and D.-G. Welsch, *Quantum Optics* (John Wiley & Sons, 2006).

[37] Hui Wang, Yu He, Yu-Huai Li, *et al.*, "Multi-photon boson-sampling machines beating early classical computers", arXiv:1612.06956 (2016)

[38] Iman Esmaeil Zadeh, Johannes W. N. Los, Ronan B. M. Gourgues, *et al.*, "Single-photon detectors combining ultra-high efficiency, detection-rates, and timing resolution", APL Photonics **2**, 111301 (2017);

[39] M. A. Nielsen and I. L. Chuang, *Quantum Computation and Quantum Information* (Cambridge University Press, Cambridge, 2000).

[40] P. Kok and B. Lovett, *Introduction to optical quantum information processing* (Springer, 2011).

[41] K. T. Kapale and J. P. Dowling, "Bootstrapping Approach for Generating Maximally Path-Entangled Photon States", Phys. Rev. Lett. **99**, 053602 (2007).

[42] B. Yurke, "Input States for Enhancement of Fermion Interferometer Sensitivity", Physical review letters **56**, 1515 (1986).

[43] H. P. Yuen, "Generation, Detection, and Application of High-Intensity Photon-Number-Eigenstate Fields", Physical review letters **56**, 2176 (1986).

[44] J. P. Dowling, "Correlated input-port, matter-wave interferometer: Quantum-noise limits to the atom-laser gyroscope", Physical Review A **57**, 4736 (1998).

[45] C. C. Gerry and R. Campos, "Generation of maximally entangled photonic states with a quantum-optical Fredkin gate", Physical Review A **64**, 063814 (2001).

[46] M. Stobinska, P. P. Rohde, and P. Kurzynski "Quantum leap: how to complete a quantum walk in a single step", (2015), `arXiv:1504.05480`.

[47] E. Knill, R. Laflamme, and G. Milburn, "A scheme for efficient quantum computation with linear optics", Nature (London) **409**, 46 (2001).

[48] M. Cooper, L. J. Wright, C. Söller, *et al.*, "Experimental generation of multi-photon Fock states ", Opt. Ex. **21**, 5309 (2013).

[49] M. A. Finger, T. S. Iskhakov, N. Y. Joly, *et al.*, "Raman-Free, Noble-Gas-Filled Photonic-Crystal Fiber Source for Ultrafast, Very Bright Twin-Beam Squeezed Vacuum", Physical review letters **115**, 143602 (2015).

[50] R. Raussendorf and H. J. Briegel, "A One-Way Quantum Computer", Phys. Rev. Lett. **86**, 5188 (2001).

[51] R. Raussendorf, D. E. Browne, and H. J. Briegel, "Measurement-based quantum computation on cluster states", Phys. Rev. A **68**, 022312 (2003).

[52] P. P. Rohde and S. D. Barrett, "Strategies for the preparation of large cluster states using non-deterministic gates", New J. Phys. **9**, 198 (2007).

[53] M. A. Nielsen, "Optical Quantum Computation Using Cluster States", Phys. Rev. Lett. **93**, 040503 (2004).

[54] D. Gross, K. Kieling, and J. Eisert, "Potential and limits to cluster-state quantum computing using probabilistic gates", Phys. Rev. A **74**, 042343 (2006).

[55] P. P. Rohde and T. C. Ralph, "Frequency and temporal effects in linear optical quantum computing", Phys. Rev. A **71**, 032320 (2005).

[56] P. P. Rohde and T. C. Ralph, "Error models for mode mismatch in linear optics quantum computing", Phys. Rev. A **73**, 062312 (2006).

[57] P. P. Rohde, T. C. Ralph, and W. J. Munro, "Practical limitations in optical entanglement purification", Phys. Rev. A **73**, 030301(R) (2006).

[58] P. P. Rohde, W. Mauerer, and C. Silberhorn, "Spectral structure and decompositions of optical states, and their applications", New J. Phys. **9**, 91 (2007).

[59] E. Knill, R. Laflamme, and G. J. Milburn, "A scheme for efficient quantum computation with linear optics," *Nature* (London) **409**, 46 (2001).

[60] P. Kok, W. J. Munro, K. Nemoto, *et al.*, "Linear optical quantum computing with photonic qubits," *Rev. Mod. Phys.* **79**, 135 (2007).

[61] L. Cohen, D. Istrati, L. Dovrat, *et al.*, "Super-resolved phase measurements at the shot noise limit by parity measurement," *Opt. Exp.* **22**, 11945 (2014).

[62] Y. Israel, S. Rosen, and Y. Silberberg, "Supersensitive polarization microscopy using NOON states of light," *Phys. Rev. Lett.* **112**, 103604 (2014).

[63] C. C. Gerry, J. Mimih, and A. Benmoussa, "Maximally entangled coherent states and strong violations of Bell-type inequalities," *Phys. Rev. A* **80**, 022111 (2009).

[64] T. Horikiri and T. Kobayashi, "Decoy state quantum key distribution with a photon number resolved heralded single photon source," *Phys. Rev. A* **73**, 032331 (2006).

[65] R. H. Hadfield, "Single-photon detectors for optical quantum information applications," *Nat. Photonics* **3**, 696 (2009).

[66] B. Dolgoshein, V. Balagura, P. Buzhan, *et al.*, "Status report on silicon photomultiplier development and its applications," *Nucl. Instrum. Methods* 563 **2**, 368 (2006).

[67] M. J. Fitch, B. C. Jacobs, T. B. Pittman, *et al.*, "Photon-number resolution using time-multiplexed single-photon detectors," *Phys. Rev. A* **68**, 043814 (2003).

[68] A. Migdall, S. V. Polyakov, J. Fan, *et al.*, *Single-Photon Generation and Detection: Physics and Applications* (Vol. 45). Academic Press. (2013).

[69] D. N. Klyshko, "Utilization of vacuum fluctuations as an optical brightness standard," *Sov. J. Quantum Electron.* **7**, 591 (1977).

[70] G. Kitaeva, A. N. Penin, V. V. Fadeev, *et al.*, "Measurement of brightness of light fluxes using vacuum fluctuations as a reference," *Sov. Phys Dokl.* **24**, 564 (1979).

[71] J. Peřina, Jr., O. Haderka, A. Allevi, *et al.*, 'Absolute calibration of photon-number-resolving detectors with an analog output using twin beams," *Appl. Phys. Lett.* **104**, 041113 (2014).

[72] A. P. Worsley, H. B. Coldenstrodt-Ronge, J. S. Lundeen, *et al.*, "Absolute efficiency estimation of photon-number-resolving detectors using twin beams," *Opt. Exp.* **17**, 4397 (2009).

[73] A. Avella, G. Brida, I. P. Degiovanni,*et al.*, "Self consistent, absolute calibration technique for photon number resolving detectors," *Opt. Exp.* **19**, 23249 (2011).

[74] X.-H. Chen, Y.-H. Zhai, D. Zhang, *et al.*,"Absolute self-calibration of the quantum efficiency of single-photon detectors," *Opt. Lett.* **31** 2441 (2006).

[75] L. Cohen, Y. Pilnyak, D. Istrati, N. M. Studer, J. P. Dowling, H. S. Eisenberg, "Absolute self-calibration of single-photon and multiplexed photon-number-resolving detectors," *Phys. Rev. A*, **94** ,012344 (2016).

[76] M. López, H. Hofer, and S. Kück, "Detection efficiency calibration of single-photon silicon avalanche photodiodes traceable using double attenuator technique," *J. Mod. Opt.* **62** (2015).

[77] L. Dovrat, M. Bakstein, D. Istrati, *et al.*, "Measurements of the dependence of the photon-number distribution on the number of modes in parametric down-conversion," *Opt. Exp.* **20**, 2266 (2010).

[78] L. Dovrat, M. Bakstein, D. Istrati, *et al.*, "Simulations of photon detection in silicon photomultiplier number-resolving detectors," *Phys. Scr.* **T147**, 014010 (2012).

[79] B.E.A Saleh and M. C. Teich, *Fundamentals of photonics*, New York: Wiley (1991)

[80] H. Paul, P. Törmä, T. Kiss, *et al.*, "Photon Chopping: New Way to Measure the Quantum State of Light," *Phys. Rev. Lett.* **76**, 2464 (1996).

[81] Eric W. Weisstein, "Stirling Number of the Second Kind." *Wolfram MathWorld*

[82] P. Buzhan, B. Dolgoshein, L. Filatov, *et al.*, "Large area silicon photonmultipliers: Performance and applications," *Nucl. Instrum. Methods* **567**, 78 (2006).

[83] I. Afek, A. Natan, O. Ambar, *et al.*, "Quantum state measurements using multipixel photon detectors," *Phys. Rev. A* **79**, 043830 (2009).

[84] M. Akiba, K. Tsujino, K. Sato, *et al.*, "Multipixel silicon avalanche photodiode with ultralow dark count rate at liquid nitrogen temperature," *Opt. Exp.* **17**, 16885 (2009).

[85] P. Eraerds, M. Legré, A. Rochas,*et al.*, "SiPM for fast Photon-Counting and Multiphoton Detection," *Opt. Exp.* **15**, 14539 (2007).

Appendix A   Sub Shot-noise Metrology in Boson-Samplers

A.1   Proof of Optimality

Here we link the analysis in MORDOR to the quantum Fisher information formalism and point out that the measurement strategy employed is optimal. To start, we calculate the probability that all photons exit the same mode that they enter,

$$
\begin{aligned}
p(k,\ldots,k) \\
= \left| \langle k |^{\otimes m} \hat{V}^{-1} [\mathbb{I} + i\varphi \hat{H} - \varphi^2 \hat{H}^2/2 - i\mathcal{O}(\varphi^3)] \hat{V} | k \rangle^{\otimes k} \right|^2 \\
= \left| 1 + i\varphi \langle \hat{H} \rangle - \varphi^2 \langle \hat{H}^2 \rangle/2 - i\mathcal{O}(\varphi^3)] \right|^2 \\
= 1 - \varphi^2 \big(\langle \hat{H} \rangle^2 - \langle \hat{H}^2 \rangle \big) + \mathcal{O}(\varphi^4) \\
= 1 - \varphi^2 \mathcal{F}(|\psi\rangle)/4 + \mathcal{O}(\varphi^4),
\end{aligned}
\tag{A.1}
$$

where we have denoted the unitary performed by the linear optical network as $\hat{V}$. Entering $p(k,\ldots,k)$ into the error propagation formulae,

$$
\Delta\varphi = \frac{\sqrt{P^2 - P}}{\left| \frac{\partial P}{\partial \varphi} \right|},
\tag{A.2}
$$

and evaluating at $\varphi = 0$ gives,

$$
\Delta\varphi = \frac{1}{\sqrt{\mathcal{F}(|\psi\rangle)}}.
\tag{A.3}
$$

Hence, this measurement basis is optimal as the Quantum Cramér-Rao bound is saturated.

In fact, in a footnote in Ref. [24] it was noted that a measurement strategy, which projected onto the state $\exp(i\varphi \hat{H})|\psi\rangle$, would indeed be optimal. This is effectively the measurement, which is being performed in the MORDOR framework making an explicit calculation, as shown here, somewhat redundant.

A.2 $\Delta\varphi$ via Matrix Permanents

Here, we summarize how matrix permanents can be used to compute the phase sensitivity $\Delta\varphi$ of an interferometer of the form of Fig. 2.1. We wish to numerically compute the probability P of measuring a single photon in each mode, which is the observable $\langle\hat{O}\rangle$ by which we obtain an estimate of φ. Since the input state and measurement is fixed across every strategy, we can use the result of Ref. [15] to compute $P = |\text{perm}(\hat{U})|^2 = |\text{perm}(\hat{V}\hat{\Phi}\hat{V}^\dagger)|^2$, where $\text{perm}(\cdot)$ refers to the matrix permanent given by the equation,

$$\text{perm}(\hat{U}) = \sum_{\sigma\in S_n}\prod_{i=1}^{n}u_{i,\sigma(i)} \; , \tag{A.4}$$

S_n being the symmetric group of degree n. The phase sensitivity $\Delta\varphi$ is then found by applying the formula for standard error propagation as in Eq. (2.2), which can be rewritten in terms of P as,

$$\Delta\varphi = \frac{\sqrt{P - P^2}}{\left|\frac{dP}{d\varphi}\right|}. \tag{A.5}$$

A.3 Optimal State Preparation

Here we calculate the QFI for the MORDOR setup with k photons entering each mode and the phase shift confined to a single mode. As before, let $\hat{V} = \hat{V}_1 = \hat{V}_2^\dagger$. Putting the phase shift in the first mode, the QFI can be calculated using the Heisenberg picture. Labelling the modes in between $\hat{V}$ and $V^\dagger$ as b_i, where $i = 1, 2, \ldots m$, then the generator of the phase shift is $\hat{H} = \hat{b}_1^\dagger\hat{b}_1$. By utilising $\hat{b}_i^\dagger = \sum_j V_{i,j}\hat{a}_j^\dagger$, it is clear that only the top row of V is important.

Now we evaluate,

$$\langle\psi|\hat{b}_1^\dagger\hat{b}_1\hat{b}_1^\dagger\hat{b}_1|\psi\rangle$$

$$= \sum_{i,j,q,l} V_{1,i}\bar{V}_{1,j}V_{1,q}\bar{V}_{1,l}\langle k|^{\otimes m}\hat{a}_i^\dagger\hat{a}_j\hat{a}_q^\dagger\hat{a}_l|k\rangle^{\otimes m}$$

$$= \sum_{q,l,q\neq l} |V_{1,q}|^2|V_{1,l}|^2\langle k|^{\otimes m}\hat{a}_l^\dagger\hat{a}_q\hat{a}_q^\dagger\hat{a}_l|k\rangle^{\otimes m}$$

$$+ \sum_{q,l} |V_{1,q}|^2|V_{1,l}|^2\langle k|^{\otimes m}\hat{a}_l^\dagger\hat{a}_l\hat{a}_q^\dagger\hat{a}_q|k\rangle^{\otimes m} \qquad (A.6)$$

$$= \sum_{q,l,q\neq l} |V_{1,q}|^2|\bar{V}_{1,l}|^2 k(k+1) + k^2$$

$$= \sum_q \left(1 - |V_{1,q}|^2\right)|\bar{V}_{1,q}|^2 k(k+1) + k^2$$

$$= \left(1 - \sum_q |V_{1,q}|^4\right)k(k+1) + k^2,$$

and similarly,

$$\langle\psi|\hat{b}_1^\dagger\hat{b}_1|\psi\rangle = \sum_{q,l} V_{1,q}\bar{V}_{1,l}\langle k|^{\otimes m}\hat{a}_q^\dagger\hat{a}_l|k\rangle^{\otimes m}$$

$$= \sum_q |V_{1,q}|^2\langle k|^{\otimes m}\hat{a}_q^\dagger\hat{a}_q|k\rangle^{\otimes m} \qquad (A.7)$$

$$= k.$$

The QFI is,

$$4\left(1 - \sum_q |V_{1,q}|^4\right)k(k+1). \qquad (A.8)$$

So to maximise the QFI, $\sum_q |V_{1,q}|^4$ should be minimized, which is achieved for $|V_{1,q}| = 1/\sqrt{m}$ giving a QFI of,

$$4\left(1 - 1/m\right)k(k+1). \qquad (A.9)$$

When the number of modes equals two this reduces to the case studied by Holland and Burnett [28]. We note that the only part of V, which played a role in this calculation was the magnitudes of the elements in the top row. Therefore, instead of a QFT circuit, a series of $m-1$ beamsplitters will also be optimal.

A.4 Derivation of $\Delta\varphi$

In order to derive the analytic form of $\Delta\varphi$ from Eq. (A.5), we first need the matrix entries of the entire network $\hat{U} = \hat{V}\hat{\Phi}\hat{V}^\dagger$. For a single unknown phase shift φ in the first mode, $\hat{\Phi}$ has the matrix form,

$$\Phi_{j,k} = \delta_{j,k}(e^{i\varphi})^{\delta_{j,1}}. \tag{A.10}$$

Although any choice of uniform $\hat{V}$, such that $|V_{j,1}| = 1/\sqrt{n}$, should be optimal for sensitivity, for this derivation we will choose $\hat{V}$ to be the n-multi-mode Quantum Fourier Transform Interferometer (QuFTI), which shares this property. The matrix entries of the entire network become,

$$
\begin{aligned}
U_{j,k} &= (V\Phi V^\dagger)_{j,k} \\
&= \sum_{l,m=1}^{n} V_{j,l}\Phi_{l,m}V^\dagger_{m,k} \\
&= \sum_{l,m=1}^{n} \underbrace{\frac{1}{\sqrt{n}}\omega_n^{(j-1)(l-1)}}_{V_{j,l}} \underbrace{\delta_{l,m}e^{i\varphi\delta_{l,1}}}_{\Phi_{l,m}} \underbrace{\frac{1}{\sqrt{n}}\omega_n^{(m-1)(1-k)}}_{V^\dagger_{m,k}}
\end{aligned}
$$

$$
\begin{aligned}
&= \frac{1}{n}\left[e^{i\varphi} + \sum_{l=2}^{n}\omega_n^{(j-1)(l-1)}\omega_n^{(l-1)(1-k)}\right] \\
&= \frac{1}{n}\left[e^{i\varphi} + \sum_{l=2}^{n}(\omega_n^{(j-k)})^{(l-1)}\right] \\
&= \frac{1}{n}\left[e^{i\varphi} + \sum_{l=1}^{n-1}(\omega_n^{(j-k)})^{l}\right] \tag{A.11}
\end{aligned}
$$

$$
= \begin{cases} \dfrac{1}{n} \left[e^{i\varphi} + n - 1 \right] & j = k \\[4mm] \dfrac{1}{n} \left[e^{i\varphi} - 1 \right] & j \neq k \end{cases}
$$

$$
= \frac{1}{n} \left[e^{i\varphi} + (\delta_{j,k}) n - 1 \right]. \tag{A.12}
$$

For $j = k$, it is easy to see the sum in Eq. (A.11) should be $n - 1$ since each term is simply $1^l = 1$. For $j \neq k$, the result follows from the fact that the sum of all n^{th} roots of unity is zero,

$$
0 = \sum_{l=1}^{n} \omega_n^l. \tag{A.13}
$$

The proof for the above follows directly from the geometric series, and it easy to see that it extends to a sum over $\omega_n^{(j-k)}$ as well.

Now that we have the matrix entries of the network, we can compute the permanent of $\hat{U} = \hat{V} \hat{\Phi} \hat{V}^{\dagger}$ which is, by definition,

$$
\text{perm}(\hat{U}) = \sum_{\sigma \in S_n} \prod_{j=1}^{n} \frac{1}{n} \left[e^{i\varphi} + (\delta_{j,\sigma(j)}) n - 1 \right]
$$

$$
= \frac{1}{n^n} \sum_{\sigma \in S_n} \prod_{j=1}^{n} \left[e^{i\varphi} + (\delta_{j,\sigma(j)}) n - 1 \right]. \tag{A.14}
$$

Suppose σ_k is some permutation with k fixed points, recalling that a *fixed point* of a permutation σ is a value $j \in \{1, .., n\}$ such that $\sigma(j) = j$ (also referred to as a *partial derangement*), then the product $\prod_{j=1}^{n}$ in Eq. (A.14) corresponding to σ_k is,

$$
\prod_{j=1}^{n} \left[e^{i\varphi} + (\delta_{j,\sigma_k(j)}) n - 1 \right] = [e^{i\varphi} + n - 1]^k [e^{i\varphi} - 1]^{n-k}. \tag{A.15}
$$

The sum in Eq. (A.14) can now be rewritten in terms of a sum over the number of fixed

points in a permutation, whose coefficient $D_{n,k}$ enumerates all permutations in S_n with k fixed points. The quantities $D_{n,k}$ are referred to as the *rencontres* numbers,

$$D_{n,k} = \frac{n!}{k!} \sum_{j=0}^{n-k} \frac{(-1)^j}{j!}. \tag{A.16}$$

The permanent is thus,

$$\text{perm}(\hat{U}) = \frac{1}{n^n} \sum_{k=0}^{n} D_{n,k} [e^{i\varphi} + n - 1]^k [e^{i\varphi} - 1]^{n-k}. \tag{A.17}$$

We are mostly interested in the behavior of $\text{perm}(\hat{U})$ for small φ, where the phase sensitivity is optimal. To simplify the remaining calculations, we focus our attention on the Taylor expansion of $F_n[\varphi] = \text{perm}(\hat{U})$ around the point $\varphi = 0$, up to second order,

$$F_n[\varphi] \approx F_n[0] + F_n'[0]\varphi + \frac{1}{2} F_n''[0] \varphi^2. \tag{A.18}$$

We can find $F_n[0]$ easily by noting that, because of the product with $[e^{i\varphi} - 1]^{n-k}$ the only non-zero term in Eq. (A.17) corresponds to $k = n$,

$$F_n[0] = \frac{1}{n^n} D_{n,n} \cdot [1 + n - 1]^n = 1. \tag{A.19}$$

Similarly, the only non-zero terms in $F_n'[0]$ must be derivatives of either $k = n$ or $k = n - 1$. Since $D_{n,n-1} = 0$, we need only concern ourselves with the derivative of the $k = n$ term.

Applying the chain rule gives,

$$F'_n[0] = \left[\frac{1}{n^n} D_{n,n}[e^{i\varphi} + n - 1]^n\right]'_{\varphi=0}$$

$$= \left[\frac{1}{n^n} D_{n,n} n[e^{i\varphi} + n - 1]^{n-1} i e^{i\varphi}\right]_{\varphi=0} \tag{A.20}$$

$$= \left[\frac{1}{n^n} \cdot 1 \cdot n[1 + n - 1]^{n-1} \cdot i\right] \tag{A.21}$$

$$= \frac{n^n}{n^n} \cdot i$$

$$= i. \tag{A.22}$$

Evaluating $F''_n[0]$ is only marginally more difficult. The $k = n$ term can be evaluated by straightforward application of the product rule to Eq. (A.20). Also, although the second derivative of the $k = n - 2$ term may be non-zero and contains a product, it is only so for the second derivative of $[e^{i\varphi} - 1]^2$—the other terms originating from the product rule are zero.

Hence, $F_n''[0]$ has only three non-zero terms,

$$
\begin{aligned}
F_n''[0] &= \left[\frac{1}{n^n} D_{n,n} n[e^{i\varphi} + n - 1]^{n-1} i e^{i\varphi}\right]'_{\varphi=0} \\
&\quad + \left[\frac{1}{n^n} D_{n,n-2}[e^{i\varphi} + n - 1]^{n-2}[e^{i\varphi} - 1]^2\right]''_{\varphi=0} \\
&= \left[\frac{1}{n^n} D_{n,n} n(n-1)[e^{i\varphi} + n - 1]^{n-2}(ie^{i\varphi})^2\right]_{\varphi=0} \\
&\quad + \left[\frac{1}{n^n} D_{n,n} n[e^{i\varphi} + n - 1]^{n-1}(ie^{i\varphi})^2\right]_{\varphi=0} \\
&\quad + \left[\frac{1}{n^n} D_{n,n-2} 2[e^{i\varphi} + n - 1]^{n-2}(ie^{i\varphi})^2\right]_{\varphi=0} \\
&= -\left[\frac{1}{n^n}(n-1)n^{n-1}\right] - \left[\frac{1}{n^n}n^n\right] \\
&\quad - \left[\frac{1}{n^n} 2 D_{n,n-2} n^{n-2}\right] \\
&= -\left[\frac{n-1}{n} + 1 + \frac{2D_{n,n-2}}{n^2}\right] \\
&= -\left[\frac{n-1}{n} + 1 + \frac{n(n-1)}{n^2}\right] \\
&= -\left[\frac{2n-2}{n} + 1\right] \\
&= -\frac{3n-2}{n}.
\end{aligned}
\tag{A.23}
$$

Thus, Eq. (A.18) becomes the simple expression,

$$
\mathrm{perm}(\hat{U}) \approx 1 + i\varphi - \left(\frac{3n-2}{2n}\right)\varphi^2.
\tag{A.24}
$$

Recall that the probability of observing n photons, each exiting individual ports, is $P =$

$|\text{perm}(\hat{U})|^2$. For small φ, then,

$$
\begin{aligned}
P &= \left| 1 + i\varphi - \left(\frac{3n-2}{2n} \right) \varphi^2 \right|^2 \\
&= \left(1 + i\varphi - \left(\frac{3n-2}{2n} \right) \varphi^2 \right) \left(1 - i\varphi - \left(\frac{3n-2}{2n} \right) \varphi^2 \right) \\
&= 1 + i\varphi - i\varphi - 2 \left(\frac{3n-2}{2n} \right) \varphi^2 - i^2 \varphi^2 + O(\varphi^4) \\
&= 1 - \frac{2n-2}{n} \varphi^2 + O(\varphi^4).
\end{aligned}
\tag{A.25}
$$

Finally, $\Delta\varphi$ becomes,

$$
\begin{aligned}
\Delta\varphi &= \frac{\sqrt{P - P^2}}{\left| \frac{\partial P}{\partial \varphi} \right|} \\
&= \frac{\sqrt{1 - \frac{2n-2}{n}\varphi^2 - 1 + \frac{4n-4}{n}\varphi^2}}{\frac{4n-4}{n}\varphi} \\
&= \frac{\sqrt{\frac{2n-2}{n}\varphi^2}}{2 \cdot \frac{2n-2}{n}\varphi} \\
&= \frac{1}{2\sqrt{2} \cdot \sqrt{\frac{n-1}{n}}},
\end{aligned}
\tag{A.26}
$$

which is in agreement with Eq. (2.7). The ratio between $\Delta\varphi$ and the shotnoise-limited phase sensitivity for n photons is then,

$$
\frac{\Delta\varphi}{1/\sqrt{n}} = \sqrt{\frac{n^2}{8(n-1)}},
\tag{A.27}
$$

which is greater than one (i.e. gives an advantage over shotnoise) for $2 \leq n \leq 6$. This is more photons than what is experimentally available today.

Appendix B   Calibration of Single-photon Detectors

B.1   Detection Probability

We first replace the matrix products in Eq. 4.5 into summations and substitute the matrix values according to Eqs. 4.1 - 4.4:

$$P_{\det}^n(s|\eta, d, N, \tilde{x}) = \tag{B.1}$$

$$\sum_{p=0}^{N} \binom{p}{s-p} \left(\tilde{x}\left(1 - \frac{p}{N}\right)\right)^{s-p} \left(1 - \tilde{x}\left(1 - \frac{p}{N}\right)\right)^{2p-s}$$

$$\sum_{k=0}^{N} \binom{N-k}{p-k} d^{(p-k)}(1-d)^{N-p}$$

$$\sum_{m=0}^{N} \frac{1}{N^m} \binom{N}{k} k! S(m,k) \binom{n}{m} \eta^m (1-\eta)^{n-m} .$$

Now, we focus on the two last lines in Eq. B.1. We notice that $m \leq n$ and $k \leq p$, because the loss effect cannot increase the photon number and dark-counts cannot decrease it. After reorder the summations and substitute $\binom{N}{k}\binom{N-k}{p-k} = \binom{N}{p}\binom{p}{k}$ we get:

$$\binom{N}{p} \sum_{m=0}^{n} \frac{1}{N^m} \binom{n}{m} \eta^m (1-\eta)^{n-m} \tag{B.2}$$

$$\sum_{k=0}^{p} \binom{p}{k} d^{(p-k)}(1-d)^{N-p} \sum_{j=0}^{k} (-1)^{k-j} \binom{k}{j} j^m .$$

We reorder the summations in the second line, use $\binom{p}{k}\binom{k}{j} = \binom{p}{j}\binom{p-j}{k-j}$ and replace the summation index $k \rightarrow k-j$, resulting in the second line to be:

$$\sum_{j=0}^{p} \binom{p}{j} j^m \sum_{k=0}^{p-j} \binom{p-j}{k} (-1)^k d^{p-k-j}(1-d)^{N-p} . \tag{B.3}$$

The inner summation equals to $(1-d)^{N-j}(-1)^{p-j}$. Substituting this in Eq. B.2 and reordering the summations, we get:

$$\binom{N}{p}\sum_{j=0}^{p}\binom{p}{j}(1-d)^{N-j}(-1)^{p-j}\sum_{m=0}^{n}\binom{n}{m}\left(\frac{\eta j}{N}\right)^{m}(1-\eta)^{n-m}.$$

(B.4)

However the second summation is a binomial expansion and regrouping it restores the third line of Eq. 4.6. The second line remains almost as is. The only change is that we change the upper limit to s, the number of activated elements by signal photon and dark counts, as we neglect higher-order cross-talks, which means the number of cross-talks is limited by the number of already activated elements. The accurate upper limit is $\min(p, N-p)$, but we checked it numerically and the difference is negligible.

B.2   SPD Detection Probability for SV States

Substituting $N=1$ in Eq. 4.6, i.e.:

$$P_{\text{det}}^{n}(s|\eta, d, 1, \tilde{x}) = \sum_{j=0}^{p}\binom{p}{j}(-1)^{p-j}(1-d)^{1-j}(1-\eta+j\eta)^{n}.$$

(B.5)

The first summation in Eq. 4.6 vanishes as a SPD has no neighbors to cross-talk to. We write the probabilities for no detection and for one photon detection explicitly:

$$P_{\text{det}}^{n}(0|\eta, d, 1, 0) = (1-d)(1-\eta)^{n},$$

(B.6)

$$P_{\text{det}}^{n}(1|\eta, d, 1, 0) = 1 - (1-d)(1-\eta)^{n}.$$

(B.7)

The probability to have zero photon counts is just the probability to not detect n photons times the probability to not have dark-counts. The probability to get one photon detection is just the complementary probability. Next, we average over the photon statistics of the SV

state.

For a TMSV state any mode has photon statistics of $P(n) = (1-x)x^n$ where x is related to $\bar{n}$, the average photon number, by $x = \frac{\bar{n}}{1+\bar{n}}$. After combining the two modes spatially the probability for $2n$-photons is $P_{TMSV}(2n) = (1-x)x^n$. We average on the statistics and get:

$$P_{\text{det}}^{\text{TMSV}}(0|\eta, d, 1, 0) = \frac{(1-d)(1-x)}{1-x(1-\eta)^2} \, , \tag{B.8}$$

$$P_{\text{det}}^{\text{TMSV}}(1|\eta, d, 1, 0) = 1 - \frac{(1-d)(1-x)}{1-x(1-\eta)^2} \, . \tag{B.9}$$

Taking the ratio of the two last equations gives Eq. 4.8.

For a SMSV state the photon statistics is $P_{SMSV}(n) = \cos^2 \frac{n\pi}{2} \frac{n!}{2^n ((\frac{n}{2})!)^2} \frac{\tanh r^n}{\cosh r}$, where r is the squeezed parameter. After the averaging we get:

$$P_{\text{det}}^{\text{SMSV}}(0|\eta, d, 1, 0) = (1-d)\frac{1}{\sqrt{1+(2\eta-\eta^2)\bar{n}}} \, , \tag{B.10}$$

$$P_{\text{det}}^{\text{SMSV}}(1|\eta, d, 1, 0) = 1 - (1-d)\frac{1}{\sqrt{1+(2\eta-\eta^2)\bar{n}}} \, , \tag{B.11}$$

where $\bar{n} = \sinh^2 r$ is the average photon number and the hyperbolic function identities, $\cosh\left(\tanh^{-1} r\right) = \frac{1}{\sqrt{1-r^2}}$, $\cosh^2 r - \sinh^2 r = 1$, were used. Taking the ratio of the two last equations yields Eq. 4.7.

Appendix C   Copyright Information

All works contained in this document are part of American Physical Society (APS) journals. Please see the figure below regarding the APS copyright policy, taken from https://journals.aps.org/copyrightFAQ.html.

Figure C.1. The APS copyright policy regarding the use of copyrighted articles in the thesis or dissertation of an author. Note the red arrows which indicate the policies relevant to this thesis.

Vita

Nicholas Michael Studer was born in 1991 in Metairie, LA and grew up in various parts of southern Louisiana including Metairie, Baton Rouge, Mandeville, and Lacombe. He also spent some years living in Ventura, CA.

Originally a undergraduate chemistry major at the University of New Orleans (UNO), Nicholas soon discovered his desire for quantitative reasoning and natural intuition was much better suited for solving problems in physics. He promptly changed majors and ended up graduating Magna Cum Laude with a Bachelor of Science degree in Physics from UNO in 2014.

His undergraduate research with the LaACES Scientific Ballooning program led him to the host institution of the program LSU immediately upon receiving his B.S.. There he met Jonathan Dowling who immediately took him on as a researcher in the summer of 2015. In his spare time, Nick enjoys cooking, writing code for small side projects, and playing competitive online games.